Converting silicon nanoparticles into nickel iron silicide nanocrystals within molten salts for water oxidation electrocatalysis

Yang Song, Sandra Casale, Antoine Miche, David Montero, Christel Laberty-Robert, David Portehault

Converting silicon nanoparticles into nickel iron silicide nanocrystals within molten salts for water oxidation electrocatalysis

Yang Song,[a] Sandra Casale,[b] Antoine Miche,[b] David Montero,[c] Christel Laberty-Robert,[a] and David Portehault*,[a]

[a] Sorbonne Université, CNRS, Laboratoire de Chimie de la Matière Condensée de Paris (CMCP), 4 place Jussieu, F-75005, Paris, France.

E-mail: david.portehault@ sorbonne-universite.fr

[b] Sorbonne Université, CNRS, Laboratoire de Réactivité de Surface (LRS), 4 place Jussieu, F-75005, Paris, France

c Sorbonne Université, CNRS, Institut des Matériaux de Paris-Centre, IMPC, F-75005, Paris, France

We synthesize metal silicide electrocatalysts for water oxidation, by using the high reactivity of silicon nanoparticles and the unique stability and low vapor pressure of molten salt solvents. We can then perform liquid-phase synthesis under vacuum at 300–400 °C. This strategy yields FeSi, Ni_2Si, and Fe-doped Ni_2Si nanocrystals, which exhibit high electrocatalytic activity for the oxygen evolution reaction with an overpotential of 337 mV at 10 mA cm^{-2} in 0.1 M KOH for Ni_2Si doped with optimal iron content. We report high stability over 85 hours. Post mortem studies reveal a core–shell–shell nanostructure, where the core remains crystalline $Ni_{2-x}Fe_xSi$ enabling charge percolation. The outer shell of nanocrystalline $Ni_{1-x}Fe_xOOH$ acts as the electrocatalytic species. The amorphous oxide intermediate layer is specific of silicides and passivates the core against further silicon leaching. These nanostructures produced in situ provide a robust, efficient, and low-cost catalyst for water oxidation.

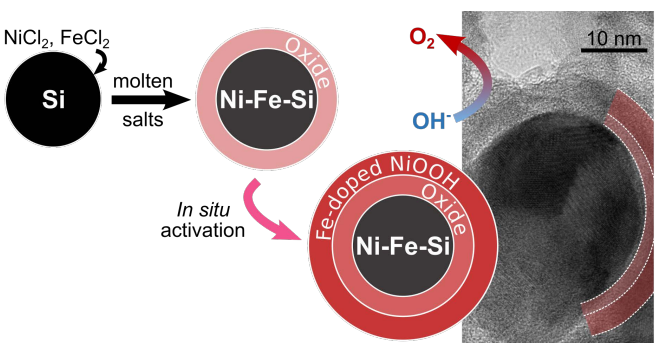

Alkaline water electrolysis has the potential to deliver dihydrogen on a large scale for chemical energy storage.[1–4] However, one of the half-reaction of water electrolysis, the oxygen evolution reaction (OER), involves a four-electron transfer hampered by kinetic factors. Electrocatalysts are then required.[5] In the present work, we explore a synthesis pathway in molten salts to design efficient silicon-based nanostructured electrocatalysts with new chemical compositions, made of earth-abundant elements.

High valence nickel and iron (NiFe)-based materials are among the most active species for OER electrocatalysis in alkaline media, delivering high electrocatalytic activities with only earth-abundant elements.[6–8] While many studies have reported the OER electrocatalysis efficiency of NiFe layered (oxy) hydroxides,[9] their layered structure exhibits moderate electrical conductivity (Table S1), together with a low surface density of active sites and a tendency towards aggregation, thus leading to fast degradation.[6,9,10] Therefore, designing composite electrodes with an electrically conductive support is required.[11–13] Most-used carbon-based supports suffer from corrosion under OER conditions, which is detrimental for performance stability.[14] Non-oxidic compounds of Ni, Fe and p-block elements such as borides,[15,16] phosphides,[17] nitrides,[18] sulfides,[19,20] and selenides[21] are possible pre-catalysts forming NiFe layered (oxy) hydroxides by *in situ* oxidation. Among these materials, some undergo only partial oxidation and are potential solutions to the electrical conductivity limitation. Indeed, by forming a thin surface layer of crystalline[20,22] or amorphous[15] metal (oxy) hydroxide/oxide under OER conditions, these materials enable charge percolation through the particle core that maintains a conductive nature.[15,20] However, the stability of such heterostructures is debatable. The existence and origin of resistance against in-depth corrosion remain to be solved.

Nickel iron silicides have never been studied as OER electrocatalysts. One can anticipate that if their oxidation during the OER was only superficial, they would deliver high electrocatalytic activity with their conductive core ($\sim 10^{-5}$ Ω cm for nickel silicides),[23,24] combined with a very low cost and low environmental impact due to the natural abundance of the constitutive elements in the Earth's crust. Designing nanostructured architectures where NiFe layered (oxy)hydroxides would be bound to a conductive silicide core, in turn protected *versus* corrosion, would enhance the surface area of the catalyst material, the electrical conductivity of the whole material, and its stability. These features can be achieved by forming core–shell nanostructures. Therefore, high performance

electrocatalysts could be achieved by developing NiFe silicide nanocrystals able to form a layered (oxy)hydroxide shell at their surface, with an interface stable against corrosion.

Besides thin films and nanowires, very few occurrences of nanostructured metal silicides have been reported.[25–28] Among them, McEnaney *et al.* obtained Cu, Pd and Ni silicide nanoparticles through a colloidal synthesis pathway.[29] Kumar *et al.* established recently a molten salt synthesis of nickel silicide nanoparticles from nickel salts and sodium silicide. Despite inadequate control of morphological features, they revealed significant OER electrocatalytic activity of materials derived from nickel silicides.[30] Nanostructured NiFe silicides are even rarer[31] and have not been studied for OER electrocatalysis, although they have been sparsely assessed for other types of catalysis, like hydrodesulfurization where Si-rich NiFe silicides were derived from silicification of nickel iron oxides.[31]

In the present work, we design metal-rich nickel iron silicide nanocrystals by exploiting (Fig. 1a) the high reactivity of nanoparticles as precursors towards nanostructured non-oxides.[32] Using nano-objects as reagents enables size and morphological control in the synthesis of multielement nano-objects when the initial objects are reacted in low temperature organic solvents.[32–36] These procedures rely mostly on metal, oxide, chalcogenide and halide nanoparticles. In this work, we use molten salts as high temperature solvents to trigger the reactivity of covalent silicon nanoparticles and convert them into size-controlled NiFe silicides. The low vapor pressure of molten salts[37,38] offers the opportunity to run liquid-phase reactions at relatively high temperature and under dynamic vacuum. This feature enables shifting the equilibrium of the reaction between metal salts and silicon nanoparticles and performing for the first time this reaction while eliminating byproducts during the synthesis. The as-obtained Fe-doped Ni_2Si nanocrystals exhibit high and stable performances in alkaline OER electrocatalysis. We then specifically address the origin of the stability of the electrochemical behavior by scrutinizing the structural and morphological changes occurring during electrocatalysis.

Results and discussion

The reactivity between metal chlorides and elemental silicon (Fig. S1 and S2) is appealing to produce metal silicides because of the low cost of these reagents and their abundancy. These reactions have been well explored by chemical vapor deposition (CVD) to yield metal silicide nanowires[25,26,28,39–42] usually at *ca.* 900 °C.[26,42] The same reaction has been performed in the solid-state and in molten salts for $CrSi_2$ at 800 °C.[43,44] This temperature is poorly compatible with the recovery of high surface area nano-objects, because of the extensive growth of these particles at high temperature. To decrease further the reaction temperature, we have used a molten salt medium to ensure liquid-phase reaction, and 40 nm silicon nanoparticles (diamond-like crystal structure, denoted as d-Si) as reagents with enhanced reactivity compared to bulk silicon. Schematically (Fig. 1a), in molten LiI-KI (eutectic molar ratio 0.63 : 0.37) with a melting point at 286 °C, the metal(II) cations were reduced by Si(0) nanoparticles and further reacted with the Si core by forming metal silicides. In the meantime, Si(0) was oxidized to Si(IV), and combined with iodides from the molten salts to form gaseous SiI_4 (boiling point at 290 °C under atmospheric pressure)[45] (see Fig. S3 for evidence of the formation of SiI_4). To ensure sample purification during the synthesis, the reaction

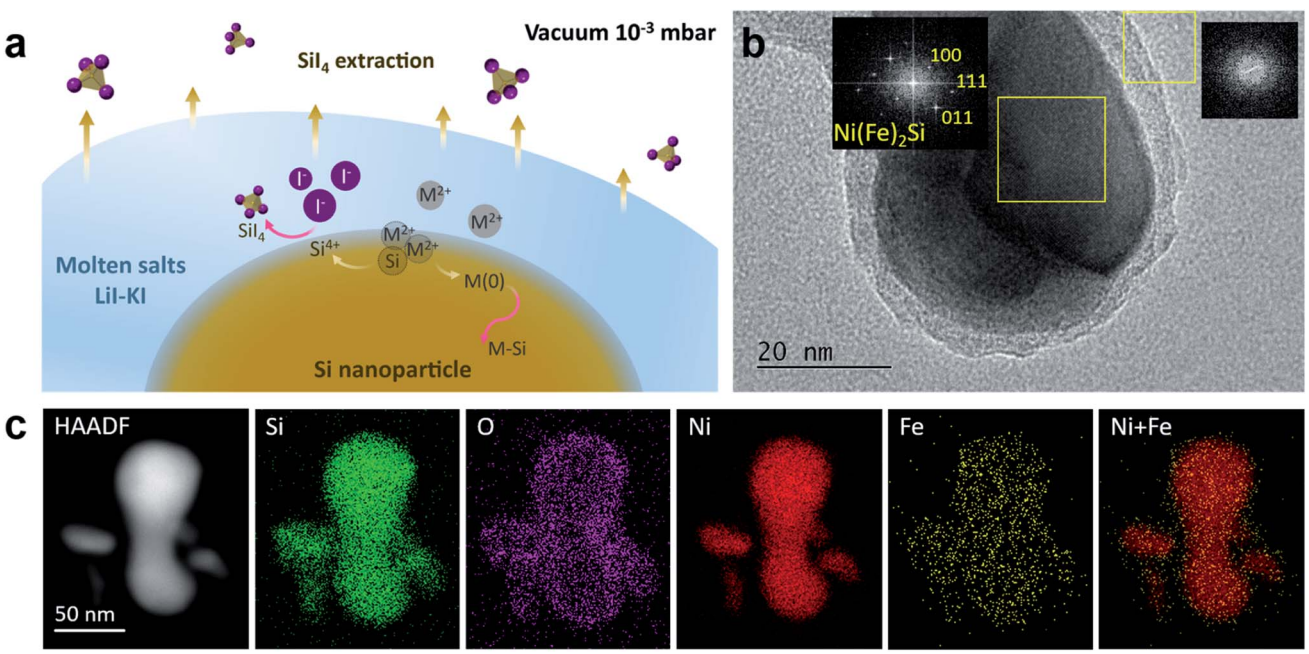

Fig. 1 (a) Schematic illustration of the reaction between Si nanoparticles and metal salts in molten salts and under vacuum. (b) HRTEM image with corresponding Fast Fourier Transform (FFT, inset) and (c) STEM-EDS chemical mapping of the as-prepared NiFeSi-12 sample. The FFT is indexed along the o-Ni_2Si structure.

was performed at 300–400 °C under dynamic vacuum (10^{-3} mbar, detailed experimental methods are described in the SI), which was made possible by the low vapor pressure of LiI–KI under the reaction conditions. At low pressure, silicon tetraiodide is extracted towards a cold trap. The synthesis under dynamic vacuum not only leads to a purified sample, it also ensures total consumption of crystalline silicon nanoparticles (Fig. S4). This demonstrates that evacuating SiI_4 shifts the reaction equilibrium. Ni_2Si and NiFe silicides (Fig. 1b, c and 2) were then obtained at 300 °C, while a higher synthesis temperature of 400 °C was required for FeSi synthesis (Fig. 2). This is consistent with the literature that reports higher formation temperature for FeSi nanowires (1100 °C) than that for Ni_2Si ones (850 °C).[28,41] In all cases, we observe a drastic decrease in the reaction temperature of at least 500 °C. Not only dynamic vacuum, but also the molten salt medium and the silicon nanoparticles play a role in this strong enhancement of reactivity, since bulk silicon reacted in molten salts (Fig. S5) or silicon nanoparticles reacted in the solid state (Fig. S6) yielded large amounts of unreacted silicon species. Therefore, we attribute the large decrease in reaction temperature to the enhanced reactivity of silicon nanoparticles *versus* bulk silicon, to the molten salt liquid medium that expedites reactions, and to the equilibrium shift under vacuum.

High resolution transmission electron microscopy (HRTEM, Fig. 1b) for the NiFeSi-12 sample (NiFeSi-*X* where *X* is the Ni : Fe ratio according to scanning electron microscopy (SEM)-energy dispersive spectroscopy analysis (EDS)) corresponding to the o-Ni_2Si structure (Fig. 2) shows the typical morphology of metal silicide nanocrystals obtained in this work. The nanoparticles with an average diameter of *ca.* 40 nm (Fig. S7) – hence a geometrical surface area of *ca.* 20 $m^2\ g^{-1}$ – exhibit a crystalline core and an amorphous native oxide layer. The amorphous oxide layer (Fig. 1b) most probably arises from exposure to air during sample preparation and storage for several days for TEM observations, which highlights the stability of the silicide core in air. All as-obtained silicide samples exhibit similar morphologies (Fig. S8), with a particle size that fits the one of the initial Si nanoparticles, thus suggesting a reaction mechanism where the metal atoms diffuse into the silicon particles, whatever the Ni/Fe ratio. According to the overlapping of the Ni, Fe and Si scanning transmission electron microscopy (STEM)-EDS maps (Fig. 1c), a homogeneous NiFe silicide is formed. STEM-EDS maps (Fig. S9) also reveal that the oxide layer is rich in Si, in agreement with the elemental compositions determined by SEM-EDS (Table S3), which indicates an excess of silicon compared to values expected from powder XRD (Fig. 2). In addition, the Ni : Fe ratios of NiFe silicides are lower than the initial reagent ratio, which suggests loss of unreacted iron during washing, in agreement with the high reaction temperature needed to incorporate iron into silicides, as observed for FeSi (Fig. 2).

According to powder XRD patterns (Fig. 2), no remaining crystalline d-Si is detected. For NiFeSi-50 and NiFeSi-12 samples, Ni_2Si is obtained primarily as the orthorhombic phase with a small fraction of the hexagonal polymorph.[46] No iron-based phase is detected, thus confirming that Fe is present as a doping agent in Ni_2Si. Upon increasing the Fe content up to Ni : Fe = 3, a mixture of FeSi and Ni_2Si crystal structures is formed. For the iron-only sample, FeSi is obtained as a pure crystalline phase.

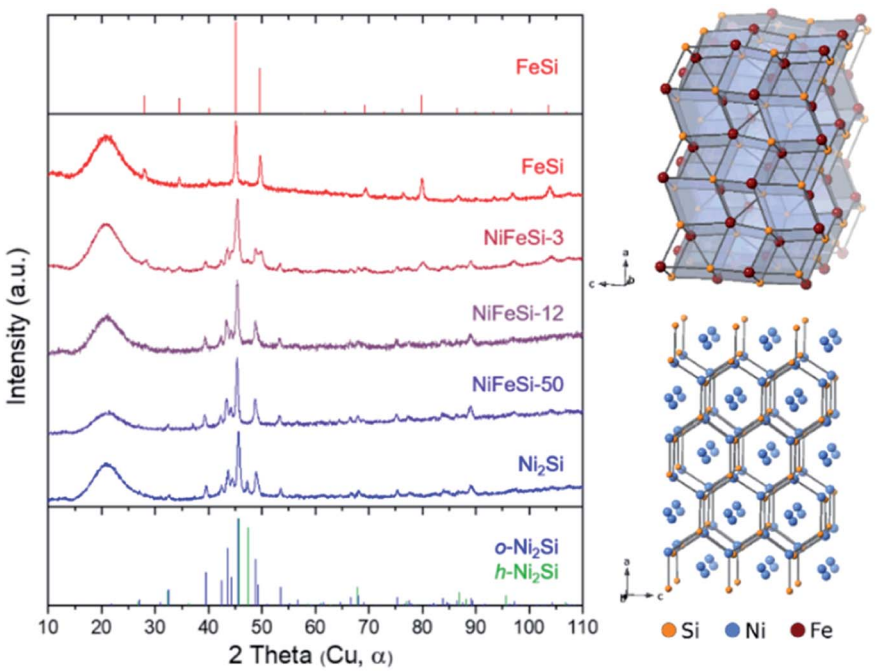

Fig. 2 XRD patterns of the as-prepared samples of Ni, Fe and NiFe silicides. The blue, green and red drop lines denote the references of o-Ni_2Si, h-Ni_2Si and FeSi, respectively. The broad bumps between 15 and 25° come from beam scattering by the protective PMMA plastic dome used for confining the Ar atmosphere around the sample. The o-Ni_2Si (bottom) and FeSi (top) crystal structures are also displayed on the right.

The chemical surface states of the NiFe silicides were analyzed by X-ray photoelectron spectroscopy (XPS) (Fig. 3). For sample NiFeSi-12, in the region of Ni $2p_{3/2}$, the peaks at 856.5 eV and 853.1 eV can be respectively ascribed to the surface oxidic Ni species and Ni–Si bonds.[30,47–49] The low energy peak only slightly shifts to higher binding energy compared to that of Ni, because the electronegativities of Ni ($\chi_{Ni} = 1.91$) and Si ($\chi_{Si} = 1.90$) are close.[50] Similarly, the Fe $2p_{3/2}$ spectrum shows two oxidation states of Fe. The peaks at 711.2 and 713.8 eV correspond to surface Fe^{3+} species,[51,52] and the peak at 707.0 eV, which is slightly higher than that of metallic Fe, fits to Fe–Si species ($\chi_{Fe} = 1.83$).[50,53,54] In the Si 2p region, the peak at 103.3 eV can be assigned to silicate or SiO_2, and the peak at 99.5 eV is characteristic of metal silicides.[55,56] Accordingly, the O 1s spectrum shows a peak at a high binding energy of 532.6 eV that can be attributed to oxidized silicon,[47] and a peak at 530.8 eV that is ascribed to the oxidized metal.[47,51]

We then assessed the electrochemical properties of NiFe silicides. In order to avoid the fortuitous influence of *in situ* Fe deposition on the catalyst activity as well as on the durability in alkaline aqueous electrolytes,[57,58] we adopted a previously reported protocol to remove the Fe impurities in KOH solution by co-precipitation of Ni and Fe as hydroxides.[57] In this work, all electrochemical measurements were performed in iron-free 0.1 M KOH (see SI for experimental details).

The electrocatalytic activity was investigated on rotating disk electrodes made of hybrid nanocrystals/Nafion films deposited on glassy carbon substrates. Although the electrocatalytic activity would be enhanced by using Ni foam substrates,[59] this configuration enables direct comparison of activities normalized *versus* the catalyst mass loading and electrode surface. With the as-prepared electrode, cyclic voltammograms (CVs) were recorded at 20 mV s^{-1}. For all silicide samples, a reversible anodic wave appearing at lower potential than the water oxidation front is attributed to the oxidation of nickel species.[57] During activation (Fig. S10), the water oxidation current increases together with the Ni oxidation/reduction wave area, which indicates that more and more Ni species are involved in this reversible redox reaction, so that the amount of high-valence Ni on the surface active for OER electrocatalysis increases. When the CVs reached a steady state, linear sweep voltammetry (LSV) was performed at 10 mV s^{-1} to probe the activated catalysts. A comparison between metal silicide nanoparticles and reference commercial IrO_2 nanoparticles is shown in Fig. 4a. The overpotentials at a current density of 10 mA cm^{-2} in 0.1 M KOH of NiFeSi-50, NiFeSi-12 and NiFeSi-3 are respectively 337, 345 and 393 mV, *versus* 440 mV for commercial IrO_2. Hence, NiFe silicides are more active than binary silicides Ni_2Si and FeSi, and exhibit activities surpassing commercial IrO_2. The overpotentials are also low compared to previously reported NiFe-based catalysts assessed under similar conditions (Table S4) and to other silicides.[30] We observe an increase in the activity with the Ni content of the three NiFe silicide samples. The potential of the Ni oxidation wave increases from *ca.* 1.45 to

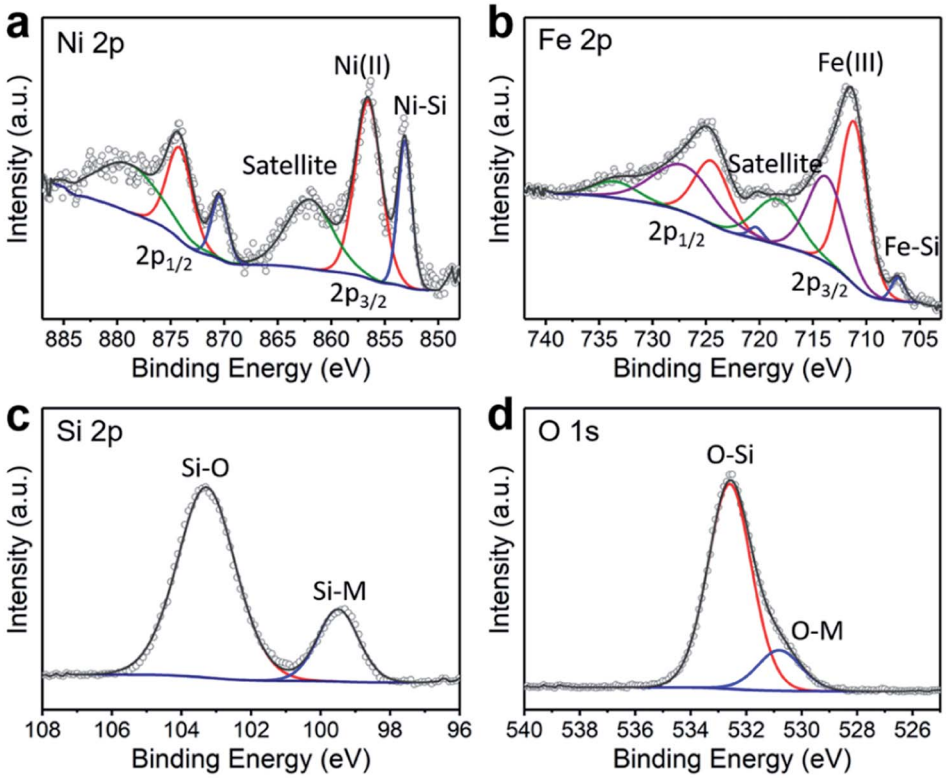

Fig. 3 XPS of the as-prepared NiFeSi-12 sample corresponding to Fe-doped Ni_2Si: (a) Ni 2p region, (b) Fe 2p region, (c) Si 2p region, and (d) O 1s region. Green curves in (a) and (b) correspond to satellites.

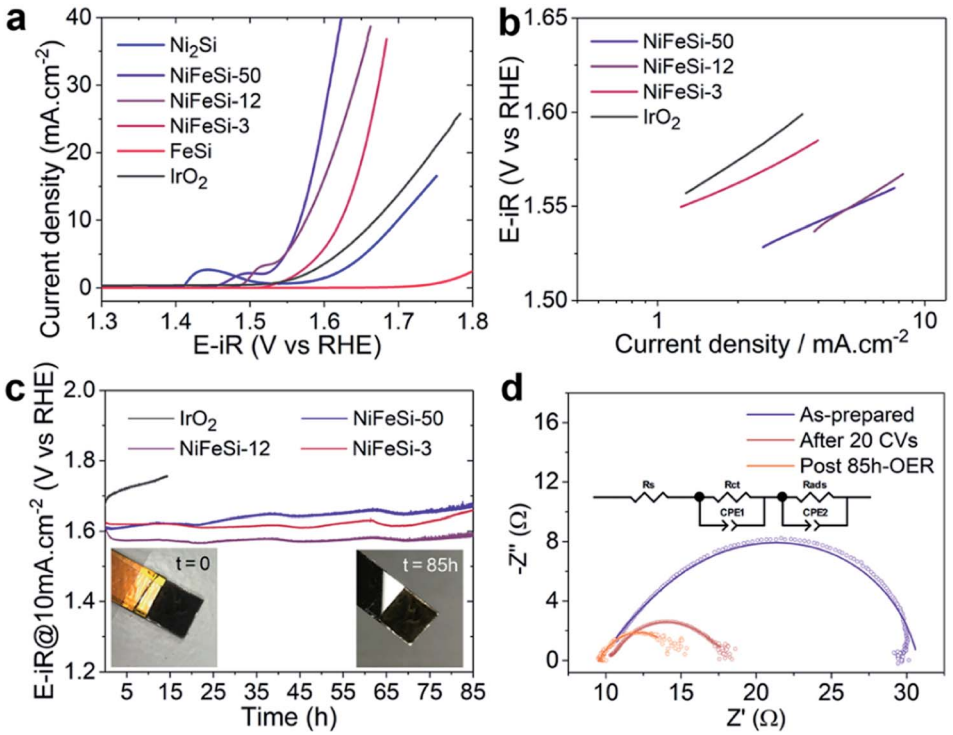

Fig. 4 OER electrocatalytic properties of metal silicide nanocrystals. (a) LSV curves of the metal silicide nanoparticles and of reference commercial IrO_2 nanoparticles in an aqueous O_2-saturated 0.1 M KOH electrolyte. (b) Tafel slopes and (c) Chronopotentiometry measurements at 10 mA cm^{-2} for NiFe silicides and IrO_2. Insets show photographs of a NiFeSi-12 working electrode with a glassy carbon substrate before and after 85 h of OER (the conductive copper foil and insulating cover were removed). (d) Nyquist plots recorded under 1.60 V *vs.* RHE and corresponding fits for NiFeSi-12 at different stages of the electrocatalytic process. The equivalent circuit is shown in the inset.

above 1.5 V *versus* the reversible hydrogen electrode (RHE) for Ni_2Si and NiFe silicides, respectively, while its area decreases from Ni_2Si to NiFe silicides, suggesting that the amount of oxidized Ni atoms is lower in NiFe silicides than in Ni_2Si. Both trends are in good agreement with previous work.[57]

The activity of NiFe silicide catalysts is confirmed by Tafel slopes (Fig. 4b). NiFeSi-50 shows the lowest Tafel slope of 63.8 mV dec^{-1}. NiFeSi-12 and NiFeSi-3 also manifest smaller Tafel slopes (85.4 and 75.3 mV dec^{-1}, respectively) than IrO_2 (95.7 mV dec^{-1}).

To evaluate the durability of the electrocatalytic activity of NiFe silicides, chronopotentiometry (CP) was carried out at 10 mA cm^{-2} (Fig. 4c) after a pre-activation step by cycling the electrode 20 times between 1.0 and 2.0 V *vs.* RHE. The reference IrO_2 used in this work was degraded in the first 15 h with a bias increment of *ca.* 85 mV, while the increments after 85 h for NiFeSi-50, NiFeSi-12 and NiFeSi-3 are *ca.* 55 mV, −35 mV and 25 mV, respectively. The most active NiFeSi-50 in LSV measurements shows the highest increment among the three NiFe silicides. This degradation could be related to Fe-leaching during the OER, which would lead to a significant decrease in the Fe content for this sample containing originally the smallest amount of iron.[11] Indeed, Fe-leaching has been identified as the main origin of deactivation for NiFe-based OER electrocatalysts.[57,58] On the opposite, the negative increment for NiFeSi-12 shows self-activation in the first 5 h. The NiFeSi-12 properties after activation demonstrate a great durability in 0.1 M KOH at 10 mA cm^{-2} for more than 85 h. The comparison of NiFe silicides with the reported NiFe-based catalysts further confirms this outstanding stability (Table S4). Moreover, NiFeSi-12 exhibits higher activity and stability than those previously reported for nickel silicide nanomaterials synthesized in molten salts.[30]

Electrochemical impedance spectroscopy (EIS) was then conducted to assess charge transport in the electrodes and at the electrode–electrolyte interfaces for silicide catalysts at different stages of the activation process (Fig. 4d). An equivalent circuit with three main components of solution resistance (R_s), charge transfer resistance (R_{ct}) and mass transfer related to reaction intermediates adsorbed at the electrode surface (R_{ads}) was used to fit EIS data.[60,61] R_{ct} decreases (Table S5) during activation, which could relate to the dissolution of the native Si-rich oxide layer. The decrease of R_{ads} indicates a more efficient adsorption/desorption process on the catalyst surface after activation.

EIS was then performed on activated silicides and IrO_2. The Nyquist plots (see Fig. S11, S12 and discussion in supplementary information) indicate that R_{ct} increases with the Fe content of NiFe silicides. This observation is consistent with the higher electrical conductivity of nickel silicides than that of iron silicides.[24,62] On the opposite, R_{ads} values (Fig. S11) are very close for the three NiFe silicides, which indicates similar surface states for these materials during electrocatalysis. The low values R_{ct} + R_{ads}

(Fig. S11) highlight the low activation barriers of charge and mass transfer in NiFe silicide catalysts and at their surface.

To elucidate the mechanisms and the origin of the high durability of electrocatalytic performances of the NiFeSi-12 sample, the corresponding electrodes were analyzed after operation at 10 mA cm^{-2} for different durations. SEM images (Fig. S13) show a roughening of the electrode surface. The XRD diagram of the post-OER electrode subjected to 10 h of OER at 10 mA cm^{-2} (Fig. S14) suggests that the main crystalline phase remains $Ni_{2-x}Fe_xSi$, although the low signal-to-background ratio due to low amounts of material does not enable identifying minor phases. Then, the elemental distribution was analyzed by STEM-EDS. The chemical maps (Fig. 5a and S15–S17) show that the outer oxidic layer of the particles is poor in Si and rich in Ni and Fe, which could be explained by the formation of a NiFe (oxy)hydroxide/oxide at the surface of the particles during the OER. This is consistent with the activation step observed in Fig. S10, *i.e.* the catalyst activation corresponds to the building of a NiFe (oxy)hydroxide/oxide layer. This observation is also in agreement with the previously reported formation of an electrocatalytically active amorphous or crystalline NiFe (oxy)hydroxide/oxide layer at the surface of NiFe borides, phosphides, nitrides and sulfides.[15,20]

Further information on the nanostructure of the catalysts was then sought by HRTEM (Fig. 5b–d). Surprisingly, the post-OER material exhibits a triple component, core–shell–shell structure. HRTEM images and the corresponding Fast Fourier Transforms (FFTs) of core areas are fully indexed along the o-Ni_2Si structure, confirming that the silicide is maintained as the main component of the material. An intermediate layer does not show any crystalline feature and is then ascribed to an amorphous phase. The outer layer exhibits many ~5 nm areas with a 2.1 Å lattice distance that can be attributed to the (105) reflection of NiOOH.[20] The outer shell then consists of Fe-doped NiOOH nanodomains.

The interface between the non-oxidic core and the oxidized shell remains clear after 85 h of OER. This confirms the stability of the nanostructure once the activation has occurred, although TEM images (Fig. 5b–d and S18) indicate that the outer oxyhydroxide shell grew thicker and rougher during the OER, while the intermediate layer barely changed in thickness. The apparent thickening of the outer hydroxide layer while the core and the intermediate layer dimensions remain steady requires a dedicated discussion. First, the increased roughness of the outer shell is consistent with the growth of nanocrystalline domains of layered NiFe oxyhydroxide. This increase in roughness yields a decrease in overall density of this shell. Second, NiFe oxyhydroxides exhibit a lower crystallographic density (~4.6 g cm^{-3}) than nickel silicide Ni_2Si (7.3 g cm^{-3}). Both features indicate that the density of the outer nanocrystalline NiFe oxyhydroxide shell is much lower than that of the nickel silicide core. Therefore, constructing the outer shell requires only small amounts of Ni and Fe from the core and then hardly impacts the size of the core. Once the outer shell is formed and crystallized, we discuss below the ability of the material to reach a steady state where further corrosion of the core is impeded by the intermediate component acting as a passivating layer.

To further understand the nature of the outer shell and of the intermediate layer, the surface chemical states were analyzed by XPS for a NiFeSi-12 working electrode as-prepared and *post mortem*, after 10 h and 85 h of OER operation. The Ni 2p spectrum of the as-prepared electrode (Fig. 6a) exhibits two peaks at 853.1 eV and 856.4 eV ascribed to Ni silicide and nickel silicate, respectively.[47–49] Accordingly, the Si 2p region (Fig. 6b) shows two peaks located at 99.6 eV and 103.5 eV attributed to silicides and oxidized silicon, respectively.[47–49] Thus, the surface chemical states of the as-synthesized powder are maintained after processing of the electrode. Beyond 10 h of OER operation, no low oxidation state Ni and Si species are detected contrary to the detection of silicides by TEM (Fig. 5). This discrepancy shows that the silicide core is out of the detection depth of XPS due to the growth of a Si-free NiFe (oxy) hydroxide shell. After 85 h of OER operation, the oxidized Ni peak slightly shifted to 856.0 eV. In the Fe 2p region (Fig. S19),

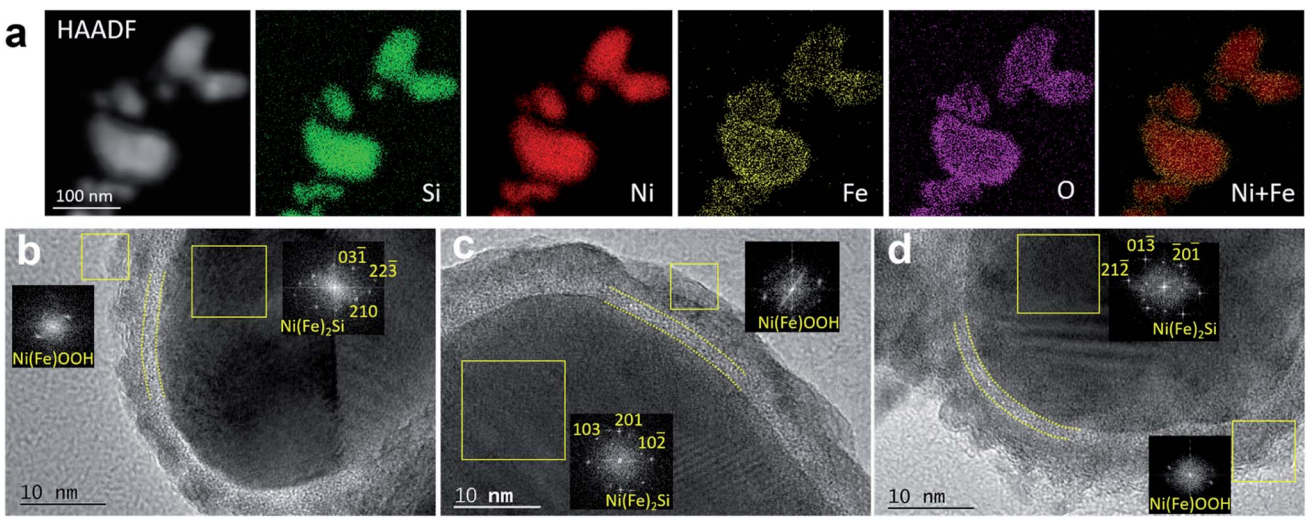

Fig. 5 (a) STEM-HAADF and STEM-EDS chemical mapping of the NiFeSi-12 catalyst post 85 h OER. HRTEM images and corresponding FFTs (insets) of the NiFeSi-12 catalyst: (b) post 10 h OER, (c) post 65 h OER, and (d) post 85 h OER.

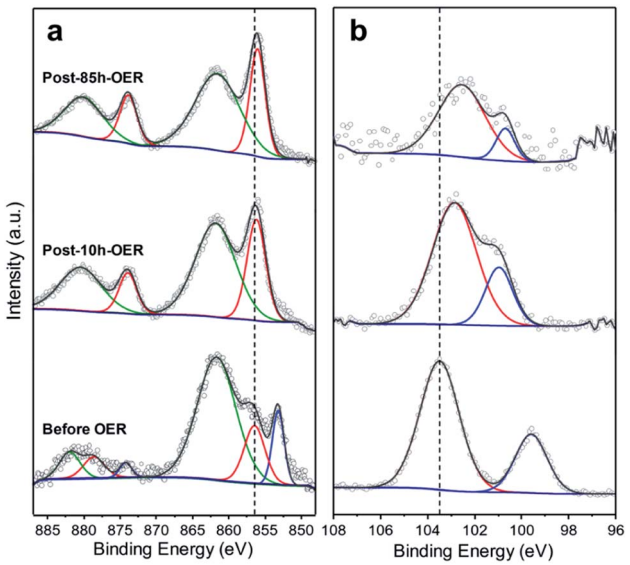

Fig. 6 XPS of a NiFeSi-12 working electrode before OER, post 10 h OER and post 85 h OER in (a) Ni 2p and (b) Si 2p regions.

Fe^{3+} species are observed. Both features suggest a chemical evolution from silicate to NiFe (oxy)hydroxide in the outer layer.[63] This is further confirmed by the decrease of the Si signal in the Si 2p region, highlighted by a decrease in the signal-to-noise ratio.

STEM-EDS maps (Fig. 5) and line profiles across the outer and intermediate layers (Fig. S20) indicate that the outer layer is mostly made of Ni and O, in agreement with XPS. From the outside of the particles to the inside, the line profiles also show an intermediate area containing Si and O besides Ni and Fe, and where the Si signal is maintained at low, but not negligible values. This observation is consistent with the attribution of the oxidic Si species detected by XPS to the amorphous intermediate layer, which then consists of metal oxide and silicates.

The overall composition of post-OER catalyst samples was also determined by SEM-EDS (Table S5). The Ni : Fe ratio does not change, while a loss of Si can be detected in the first 65 h. Nonetheless, the overall composition stabilizes after 65 h, with a (Ni + Fe)/Si ratio of 2.6, in agreement with a maintained $(Ni_{1-x}Fe_x)_2Si$ core and an outer Si-free shell of nickel iron (oxy) hydroxide. This is consistent with partial dissolution of SiO_2 or silicates[64] in 0.1 M KOH in the first 65 h. Because the composition of the electrode material does not evolve after 65 h and the conductive silicide core is maintained, the amorphous ~1.5 nm-thick intermediate layer observed by TEM (Fig. 5b–d) should play a role in passivating the silicide core and protecting it from oxidation and silicon leaching.

XPS (Fig. 6 and S19) shows that this intermediate shell contains high valence Ni and Fe, silicate and/or silicon oxide. This passivation layer generated under anodic and basic conditions can protect the silicide core from further dissolution.[65] TEM (Fig. 5b–d) also indicates that this intermediate shell is denser than the outer Fe-doped NiOOH shell, which implies further reactivity with water to form the outer oxyhydroxide shell. The intermediate layer is buried below this outer shell and is then not in contact with water. Overall, these reactivity considerations support the interpretation that this intermediate layer is a mixture of amorphous nickel oxide and silicates that may be doped with iron.

As stated in previous reports,[66] nonmetal elements P, S, Se, Te in transition metal compounds are thermodynamically unstable under anodic conditions in strongly alkaline solutions, although the kinetics of their dissolution is slow. For the materials described herein, Si leaches to form a (NiFe)OOH outer shell on the silicide particles. However, the morphology and/or composition of this shell depends on the nature of the nonmetal element. For those forming a passivating oxide layer, the core could be protected. Although further corrosion may occur if harsher conditions were applied, we stress out that the NiFe silicide-based catalysts described herein keep for the long duration of our measurements their core–shell–shell structure with a clear core–shell boundary, thus suggesting limited corrosion of the core during electrocatalysis, unlike most reported compounds of transition metal and p-block elements, for which the core/shell boundary vanishes upon OER operation.

Conclusion

We synthesized FeSi, Ni_2Si and NiFe silicide nanocrystals through a redox reaction between silicon nanoparticles and metal chlorides by designing a strategy to accelerate and achieve this reaction hundreds of degrees below the usual temperature of the solid-state reaction between bulk reagents: the high reactivity of silicon nanoparticles was combined with two specific features of molten salts, namely their ability to operate as liquid media at 300–400 °C and their low vapor pressure that enables running reactions under dynamic vacuum to shift equilibria. This synthesis strategy delivers a pathway to a wide range of nanomaterials.

The resulting NiFe silicide nanoparticles were highly active for OER electrocatalysis, with an activity stable for at least 85 h of continuous electrolysis at 10 mA cm^{-2}. These high performances arise from the NiFe silicide nanocrystals acting as precatalysts, and an electrocatalytically active crystalline Fe-doped NiOOH shell forming upon silicon leaching. The resulting nanostructures are however highly stable because of a dense oxidic intermediate layer containing metal and silicon that avoids contact of the silicide core with the electrolyte. Therefore, the metallic core can play its role of enhancing charge transfer within the electrode. This *in situ* evolution of nickel iron silicides towards core–shell–shell nanostructures with a passivating intermediate layer has not been observed yet for other metal-p block element compounds, including nickel silicides formed in molten salts. Therefore, this original behavior shows the ability to design hierarchically structured electrocatalysts built from Earth abundant elements. Furthermore, silicide-modified Si photoanodes have been investigated for photoelectrocatalysis of water splitting.[42,67,68] The NiFe silicides reported in this work demonstrate high activity and stability. They are potential candidates for further improving the

photoelectrocatalytic properties of silicide-modified Si photoanodes.

Conflicts of interest

There are no conflicts to declare.

Acknowledgements

Y. S. acknowledges the China Scholarship Council for her PhD fellowship, as well as the French state funds within the framework of the Cluster of Excellence MATISSE led by Sorbonne Université. This project has received funding from the European Research Council (ERC) Consolidator Grant GENESIS under the European Union's Horizon 2020 research and innovation programme (grant agreement no. 864850. We thank the Institut des Matériaux de Paris Centre (IMPC FR2482) for servicing FEG-SEM and (S)TEM instrumentation and Sorbonne Université, CNRS and C'Nano projects of the Région Ile-de-France for funding.

References

1 A. Ursúa, L. M. Gandía and P. Sanchis, *Proc. IEEE*, 2012, **100**, 410–426.
2 J. Brauns and T. Turek, *Processes*, 2020, **8**, 248.
3 M. M. Rashid, M. K. Al Mesfer, H. Naseem and M. Danish, *Int. J. Eng. Adv. Technol.*, 2015, **4**, 2249–8958.
4 W. Kreuter and H. Hofmann, *Int. J. Hydrogen Energy*, 1998, **23**, 661–666.
5 M. I. Jamesh and X. Sun, *J. Power Sources*, 2018, **400**, 31–68.
6 J. Zhao, J. J. Zhang, Z. Y. Li and X. H. Bu, *Small*, 2020, **16**, 1–23.
7 J. Mohammed-Ibrahim, *J. Power Sources*, 2020, **448**, 227375.
8 C. Qiao, Z. Usman, T. Cao, S. Rafai, Z. Wang, Y. Zhu, C. Cao and J. Zhang, *Chem. Eng. J.*, 2021, **426**, 130873.
9 M. Xu and M. Wei, *Adv. Funct. Mater.*, 2018, **28**, 1–20.
10 Y. Wang, D. Yan, S. El Hankari, Y. Zou and S. Wang, *Adv. Sci.*, 2018, **5**, 1800064.
11 C. Feng, M. B. Faheem, J. Fu, Y. Xiao, C. Li and Y. Li, *ACS Catal.*, 2020, **10**, 4019–4047.
12 W. Ma, R. Ma, C. Wang, J. Liang, X. Liu, K. Zhou and T. Sasaki, *ACS Nano*, 2015, **9**, 1977–1984.
13 D. Zhou, Z. Cai, X. Lei, W. Tian, Y. Bi, Y. Jia, N. Han, T. Gao, Q. Zhang, Y. Kuang, J. Pan, X. Sun and X. Duan, *Adv. Energy Mater.*, 2018, **8**, 1701905.
14 T. Joo, L. Hu, B. K. Hong, J. G. Oh and S. Litster, *J. Power Sources*, 2020, **472**, 228439.
15 W. Hong, S. Sun, Y. Kong, Y. Hu and G. Chen, *J. Mater. Chem. A*, 2020, **8**, 7360–7367.
16 L. An, Y. Sun, Y. Zong, Q. Liu, J. Guo and X. Zhang, *J. Solid State Chem.*, 2018, **265**, 135–139.
17 P. Li and H. C. Zeng, *J. Mater. Chem. A*, 2018, **6**, 2231–2238.
18 G. Fu, Z. Cui, Y. Chen, L. Xu, Y. Tang and J. B. Goodenough, *Nano Energy*, 2017, **39**, 77–85.
19 W. Chen, H. Wang, Y. Li, Y. Liu, J. Sun, S. Lee, J. S. Lee and Y. Cui, *ACS Cent. Sci.*, 2015, **1**, 244–251.
20 M. Zhou, Q. Weng, X. Zhang, X. Wang, Y. Xue, X. Zeng, Y. Bando and D. Golberg, *J. Mater. Chem. A*, 2017, **5**, 4335–4342.
21 X. Xu, F. Song and X. Hu, *Nat. Commun.*, 2016, **7**, 1–7.
22 Y. Li, H. Zhang, M. Jiang, Q. Zhang, P. He and X. Sun, *Adv. Funct. Mater.*, 2017, **27**, 1–8.
23 B. Meyer, U. Gottlieb, O. Laborde, H. Yang, J. C. Lasjaunias, A. Sulpice and R. Madar, *J. Alloys Compd.*, 1997, **262–263**, 235–237.
24 E. G. Colgan, M. Mäenpää, M. Finetti and M.-A. Nicolet, *J. Electron. Mater.*, 1983, **12**, 413–422.
25 W. L. Chiu, C. H. Chiu, J. Y. Chen, C. W. Huang, Y. T. Huang, K. C. Lu, C. L. Hsin, P. H. Yeh and W. W. Wu, *Nanoscale Res. Lett.*, 2013, **8**, 1–5.
26 A. L. Schmitt, J. M. Higgins, J. R. Szczech and S. Jin, *J. Mater. Chem.*, 2010, **20**, 223–235.
27 S. Agarwal, V. Ganesan, A. K. Tyagi and I. P. Jain, *Bull. Mater. Sci.*, 2006, **29**, 647–651.
28 J. Y. Lin, H. M. Hsu and K. C. Lu, *CrystEngComm*, 2015, **17**, 1911–1916.
29 J. M. McEnaney and R. E. Schaak, *Inorg. Chem.*, 2015, **54**, 707–709.
30 R. Kumar, M. Bahri, Y. Song, F. Gonell, C. Thomas, O. Ersen, C. Sanchez, C. Laberty-Robert and D. Portehault, *Nanoscale*, 2020, **12**, 15209–15213.
31 X. Chen, J. Wang, K. Yang, C. Meng, C. T. Williams and C. Liang, *J. Phys. Chem. C*, 2015, **119**, 29052–29061.
32 R. Buonsanti, A. Loiudice and V. Mantella, *Acc. Chem. Res.*, 2021, **54**, 754–764.
33 L. Manna, J. Cheon and R. E. Schaak, *Acc. Chem. Res.*, 2021, **54**, 1543–1544.
34 M. Saruyama, R. Sato and T. Teranishi, *Acc. Chem. Res.*, 2021, **54**, 765–775.
35 R. E. Schaak, B. C. Steimle and J. L. Fenton, *Acc. Chem. Res.*, 2020, **53**, 2558–2568.
36 S. Toso, D. Baranov and L. Manna, *Acc. Chem. Res.*, 2021, **54**, 498–508.
37 D. Portehault, S. Delacroix, G. Gouget, R. Grosjean and T. H. C. Chan-Chang, *Acc. Chem. Res.*, 2018, **51**, 930–939.
38 S. K. Gupta and Y. Mao, *J. Phys. Chem. C*, 2021, **125**, 6508–6533.
39 K. Seo, K. S. K. Varadwaj, P. Mohanty, S. Lee, Y. Jo, M. H. Jung, J. Kim and B. Kim, *Nano Lett.*, 2007, **7**, 1240–1245.
40 N. Dahal and V. Chikan, *Chem. Mater.*, 2010, **22**, 2892–2897.
41 L. Ouyang, E. S. Thrall, M. M. Deshmukh and H. Park, *Adv. Mater.*, 2006, **18**, 1437–1440.
42 X. Chen and C. Liang, *Catal. Sci. Technol.*, 2019, **9**, 4785–4820.
43 M. Godfroy, A. Russel, F. Mercier, M. Granier, T. Jarrosson, C. Niebel, F. Serein Spirau, R. Viennois and M. Beaudhuin, *Mater. Lett.*, 2019, **247**, 7–10.
44 H. F. Hsu, P. C. Tsai and K. C. Lu, *Nanoscale Res. Lett.*, 2015, **10**, 4–11.
45 W. Collins, Silicon Compounds, Silicon Halides, in *Kirk-Othmer Encyclopedia of Chemical Technology*, ed. K. Othmer,

John Wiley & Sons, 2000, DOI: 10.1002/0471238961.1909120903151212.a01.
46 TDnucl - Thermodata Nuclear Phase Diagrams, Ni-Si, https://www.crct.polymtl.ca/fact/phase_diagram.php?file=Ni-Si.jpg&dir=TDnucl.
47 R. B. Shalvoy, P. J. Reucroft and B. H. Davis, *J. Catal.*, 1979, **56**, 336–348.
48 Y. Cao, L. Nyborg and U. Jelvestam, *Surf. Interface Anal.*, 2009, **41**, 471–483.
49 P. Lorenz, J. Finster, G. Wendt, J. V. Salyn, E. K. Žumadilov and V. I. Nefedov, *J. Electron Spectrosc. Relat. Phenom.*, 1979, **16**, 267–276.
50 M. Dayah, *Ptable*, https://ptable.com.
51 P. C. J. Graat and M. A. J. Somers, *Appl. Surf. Sci.*, 1996, **100–101**, 36–40.
52 N. Nasralla, M. Yeganeh, Y. Astuti, S. Piticharoenphun, N. Shahtahmasebi, A. Kompany, M. Karimipour, B. G. Mendis, N. R. J. Poolton and L. Šiller, *Sci. Iran.*, 2013, **20**, 1018–1022.
53 P. L. Tam, Y. Cao and L. Nyborg, *Surf. Sci.*, 2012, **606**, 329–336.
54 K. Zhang, M. Brötzmann and H. Hofsäss, *AIP Adv.*, 2012, **2**, 032123.
55 J. Masa, S. Piontek, P. Wilde, H. Antoni, T. Eckhard, Y. T. Chen, M. Muhler, U. P. Apfel and W. Schuhmann, *Adv. Energy Mater.*, 2019, **9**, 1–8.
56 H. Junge, M. Beller, A. Agapova, P. Ryabchuk, H. Lund, K. Junge, G. Agostini and M.-M. Pohl, *Sci. Adv.*, 2018, **4**, eaat0761.
57 L. Trotochaud, S. L. Young, J. K. Ranney and S. W. Boettcher, *J. Am. Chem. Soc.*, 2014, **136**, 6744–6753.
58 R. Farhat, J. Dhainy and L. I. Halaoui, *ACS Catal.*, 2020, **10**, 20–35.
59 J. N. Hausmann, R. Beltrán-Suito, S. Mebs, V. Hlukhyy, T. F. Fässler, H. Dau, M. Driess and P. W. Menezes, *Adv. Mater.*, 2021, **33**, 2008823.
60 D. V. Franco, L. M. Da Silva, W. F. Jardima and J. F. C. Boodts, *J. Braz. Chem. Soc.*, 2006, **17**, 746–757.
61 J. Qi, W. Zhang, R. Xiang, K. Liu, H. Y. Wang, M. Chen, Y. Han and R. Cao, *Adv. Sci.*, 2015, **2**, 1–8.
62 S. Paschen, E. Felder, M. Chernikov, L. Degiorgi, H. Schwer, H. Ott, D. Young, J. Sarrao and Z. Fisk, *Phys. Rev. B: Condens. Matter Mater. Phys.*, 1997, **56**, 12916–12930.
63 K. K. Lian, D. W. Kirk and S. J. Thorpe, *J. Electrochem. Soc.*, 1995, **142**, 4309.
64 P. V. Brady and J. V. Walther, *Geochim. Cosmochim. Acta*, 1989, **53**, 2823–2830.
65 I. L. Rakityanskaya and A. B. Shein, *Russ. J. Electrochem.*, 2006, **42**, 1208–1212.
66 W. Li, D. Xiong, X. Gao and L. Liu, *Chem. Commun.*, 2019, **55**, 8744–8763.
67 Z. Xia, X. Zhou, J. Li and Y. Qu, *Sci. Bull.*, 2015, **60**, 1395–1402.
68 F. R. F. Fan, R. G. Keil and A. J. Bard, *J. Am. Chem. Soc.*, 1983, **105**, 220–224.

Supporting Information

Converting Silicon Nanoparticles into Nickel Iron Silicide Nanocrystals within Molten Salts for Water Oxidation Electrocatalysis

Yang Song, Sandra Casale, Antoine Miche, David Montero, Christel Laberty-Robert, David Portehault[*]

Table of contents

Electrode conductivity: comparison of related materials

Table S1 Comparison of the conductivity of reported OER electrocatalysts by their charge transfer resistances (R_{ct}) obtained from the electrochemical impedance spectroscopy (EIS).

Catalysts	R_{ct} (Ω)	Ref.
NiFeSi-12	17	This work
NiFeSi-50	5	This work
Ni-Fe disulfide	10	[1]
Ni-Fe hydroxide	17.5	[1]
$(Ni_{0.75}Fe_{0.25})_2P$	5	[2]
NiFe borate/rGO	38	[3]
NiFe borate	81	[3]
NiFe LDH/oGSH	100	[4]
NiFe LDH	1800	[4]
NiFe oxide	50	[5]
NiFe LDH/carbon network	353	[6]
NiFe LDH	875	[6]
NiFe LDH	70	[7]
$NiFe2O_4/Ni(OH)_2$	500	[8]

Chemicals

Reagents Lithium iodide (99%, Alfa Aesar), potassium iodide (99%, Sigma-Aldrich), silicon nanoparticles (99%, Nanomakers©, France), bulk Si powder (99 %, Sigma-Aldrich), nickel(II) chloride (99%, Alfa Aesar) and iron(II) chloride (99.5%, Alfa Aesar) were stored and manipulated as received in an Ar-filled glovebox (H_2O < 0.5 ppm, O_2 < 0.5 ppm). Methanol (VWR Normapur grade) was used for washing.

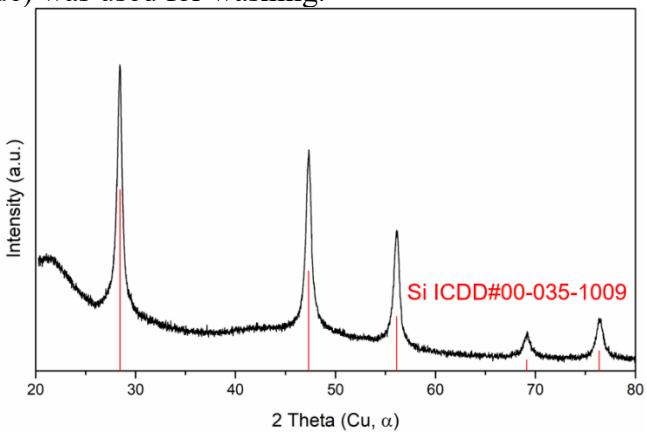

Figure S1. Powder XRD pattern of Si nanoparticles used as reagents. Red drop lines indicate a diamond-like structure Si reference.

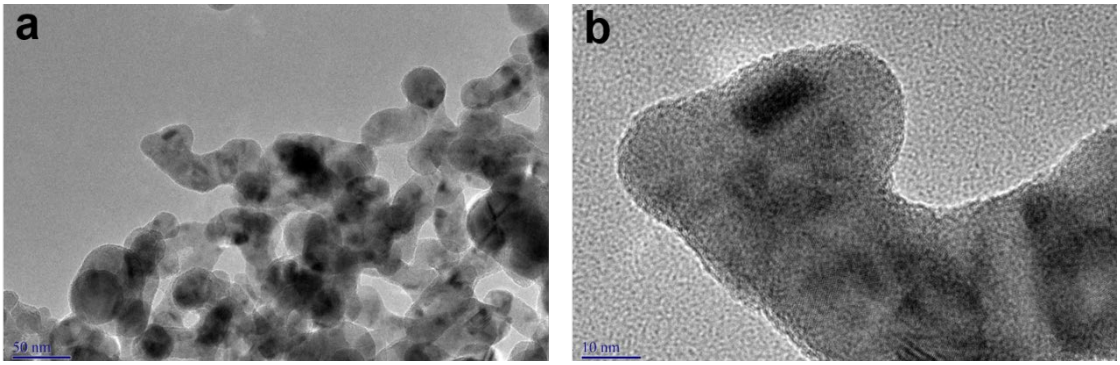

Figure S2. TEM images of Si nanoparticles used as reagents.

Instruments

Powder X-ray diffraction (XRD) diagrams were acquired on a Bruker D8 Advance diffractometer operating at the Cu Kα wavelength (λ = 1.5418 Å). *o*-Ni_2Si, *h*-Ni_2Si, FeSi, and NiOOH were identified according to the ICDD database and the reference cards 04-010-3516, 01-072-2547, 04-007-2551 and 00-06-0075 respectively.

X-ray photoelectron spectroscopy (XPS) analyses were performed using an Omicron Argus X-ray photoelectron spectrometer, equipped with a monochromated AlKα radiation source (1486.6 eV) and a 280 W electron beam power. Binding energies were calibrated against the C 1s (C-C) binding energy at 284.8 eV.

High-resolution transmission electron microscopy (HRTEM) was carried out on a JEOL JEM 2100 FEG microscope (Tokyo, Japan) operating at 200 kV with a spatial punctual resolution of 1.8 Å equipped with X-ray Energy Dispersive Spectroscopy (EDS) for chemical analysis. The samples were prepared by depositing a drop of ethanolic suspension on carbon coated Cu grids.

Analysis energy-dispersive X-ray spectroscopy (EDS) (Oxford Instruments – X-max) was performed on a scanning electron microscope (SEM) HITACHI S3400N at 20 kV. Cobalt was used for calibration of quantitative analyses. Powder samples were flatly smeared on a carbon adhesive tape on sample holder. Spectra were recorded on three to six different zones for each sample.

Scanning electron microscopy (SEM) was carried out on a Hitachi SU-70 FESEM. Postmortem electrodes were observed without any surface coating, accelerating voltage settings as indicated in images.

Synthesis method

Metal silicide nanoparticles Si nanoparticles, metal chloride $NiCl_2$, $FeCl_2$ or both, 2.9 g LiI (21.7 mmol) and 2.1 g KI (12.7 mmol) were ball-milled during 2 min at 20 Hz (Retsch MM400 ball mill airtight vial of 50 mL, filled with one steel ball of 62.3 g with a diameter of 23 mm) to get a well-mixed fine powder. Precise reactant amounts are listed in the **Table S1**. The mixture was loaded in a quartz tube (Ø28×H345 mm) which was then connected to a N_2-flowed Schlenk line. An intermediate liquid nitrogen trap between the quartz tube and the Schlenk line was set to condensate the volatile byproduct SiI_4. A vertical furnace from Eraly® was pre-heated to the reaction temperature. Afterward, the quartz tube was evacuated and placed into the furnace. The reaction medium was maintained at the targeted temperature for 6 hours under dynamic vacuum (10^{-3} mbar). Then, the hot quartz tube was taken out and cooled down to room temperature. The as-obtained mixture was washed in methanol by seven cycles of centrifugation/redispersion and was later dried in a Schlenk tube under vacuum. The resulting powder was transferred and stored in an Ar-filled glovebox. A typical synthesis yields about 100 mg of powders, which corresponds to a yield of about 90 %.

Table S2. Reactant masses, amounts and temperatures for syntheses of Ni, Fe and NiFe silicides

Samples	Reactant / mg (mmol)			Reaction temperature (°C)
	Si	$NiCl_2$	$FeCl_2$	
Ni_2Si	42.1 (1.5)	194.4 (1.5)	/	300
NiFeSi-50	52.5(1.9)	243.0 (1.9)	47.5 (0.4)	300
NiFeSi-12	42.1 (1.5)	146.0 (1.1)	47.5 (0.4)	300
NiFeSi-3	84.3(3.0)	194.4 (1.5)	190.1(1.5)	300
FeSi	63.2 (2.3)	/	190.1(1.5)	400

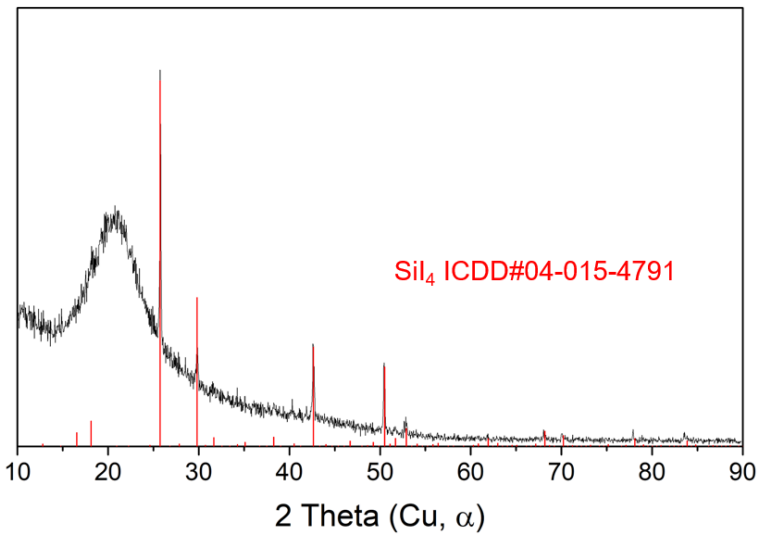

Figure S3. Powder XRD pattern of the byproduct of metal silicide synthesis, which can be indexed along the SiI_4 reference (indicated by red lines). The broad bumps between 15-25 ° come from the beam scattering of the protective PMMA plastic dome used for confining the Ar atmosphere around the sample.

Impact of synthesis parameters of Ni_2Si

Synthesis under Ar. 42.1 mg Si nanoparticles (1.5 mmol), 194.4 mg $NiCl_2$ (1.5 mmol) and 5 g LiI-KI (0.63:0.37 mol.) were ball-milled during 2 min. The same synthesis procedure was followed with the same setup as the synthesis described above, except that the reaction was under Ar flow instead of vacuum. The as-prepared solid was washed in methanol and in deionized water, respectively by six cycles and two cycles of centrifugation/redispersion, and was later dried under vacuum. The XRD diagram of final product is shown in **Figure S4**.

Synthesis from bulk Si powder. 42.1 mg bulk Si powder (1.5 mmol), 194.4 mg $NiCl_2$ (1.5 mmol) and 5 g LiI-KI (0.63:0.37 mol.) were ball-milled during 2 min. The synthesis protocol described above was kept. The as-obtained mixture was washed in methanol and in deionized water, respectively by six cycles and two cycles of centrifugation/redispersion, and was later dried under vacuum. The XRD diagram of final product is shown in **Figure S5**.

Synthesis without molten salts. 42.1 mg Si nanoparticles (1.5 mmol) and 194.4 mg $NiCl_2$ (1.5 mmol) were ball-milled during 2 min. Later, the same procedure was followed. After thermal treatment, the resulting powder was directly collected. The XRD diagram of final product is shown in **Figure S6**.

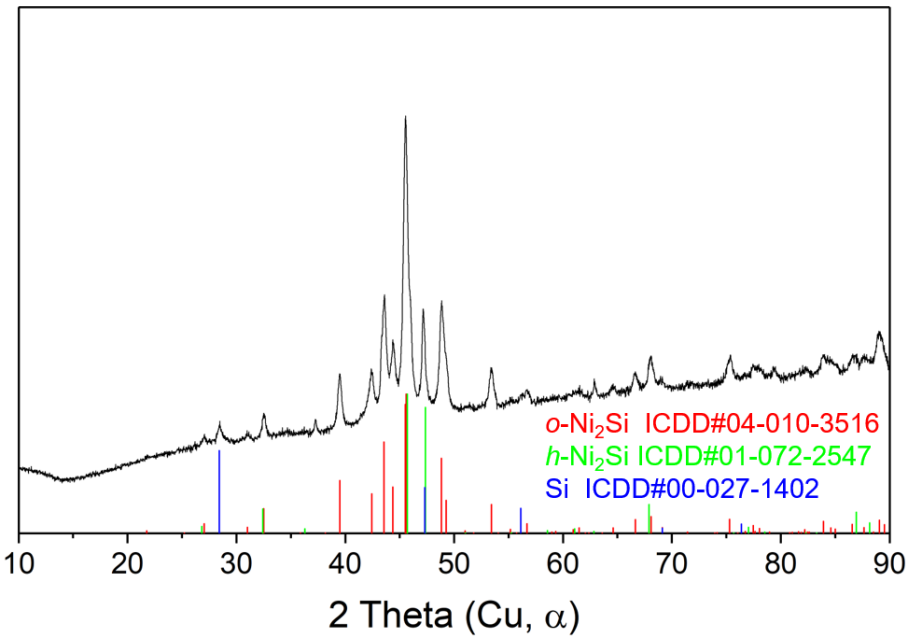

Figure S4. Powder XRD pattern of the final product from the reaction between Si nanoparticles and $NiCl_2$ under argon at 395°C for 6 hours in LiI-KI. Nickel silicides were the major phase, however unreacted Si can be observed.

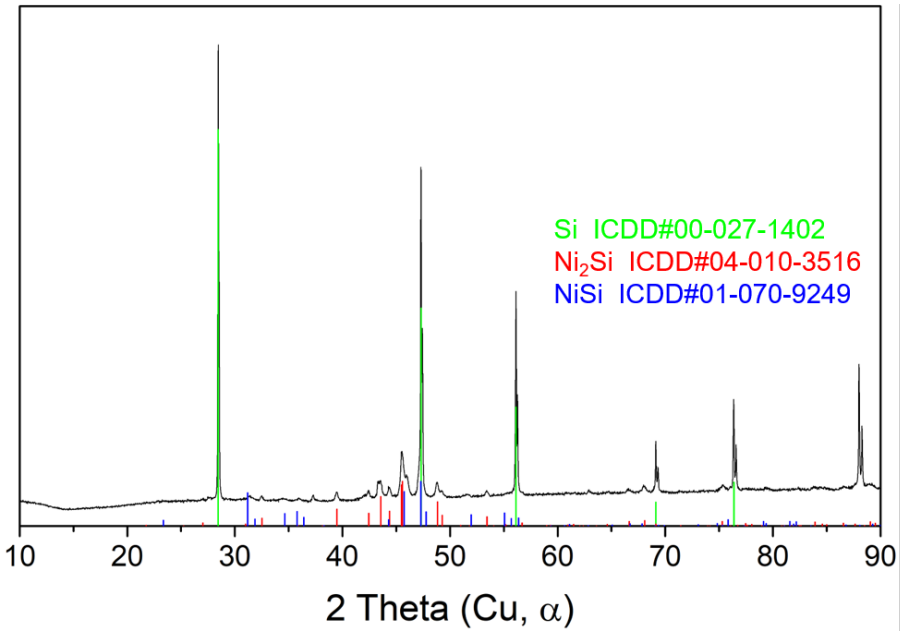

Figure S5. Powder XRD pattern of the final product from the reaction between bulk Si powder and $NiCl_2$ under vacuum at 395 °C for 6 hours in LiI-KI. Large amount of Si remains unreacted. Nickel silicides were formed in a minor fraction.

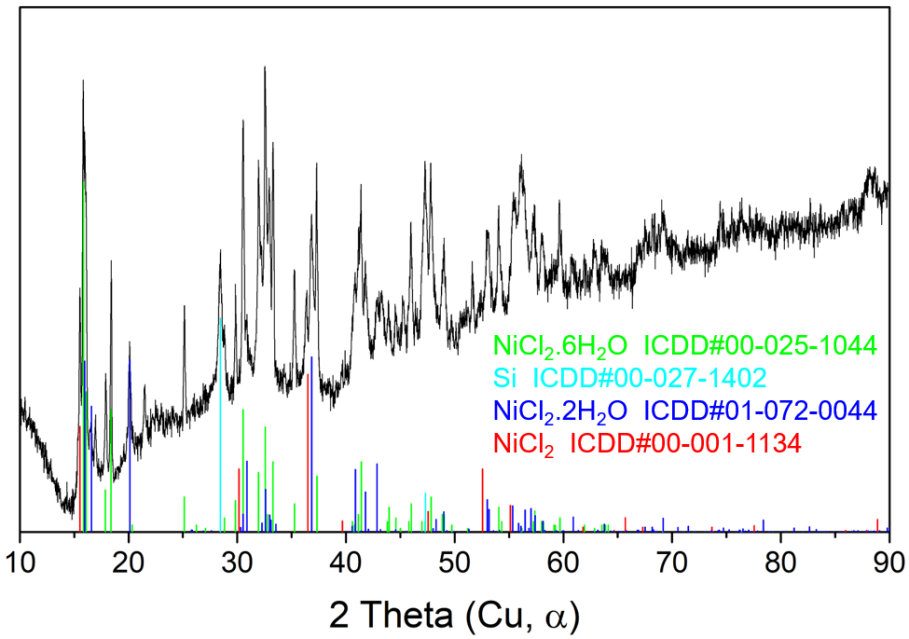

Figure S6. Powder XRD pattern of the final product from the solid-solid reaction between Si nanoparticles and $NiCl_2$ under vacuum at 395°C for 6 hours. Unreacted Si and $NiCl_2$ were found. $NiCl_2$ was hydrated because the XRD diagram was acquired in the air.

Characterization of metal silicide nanoparticles

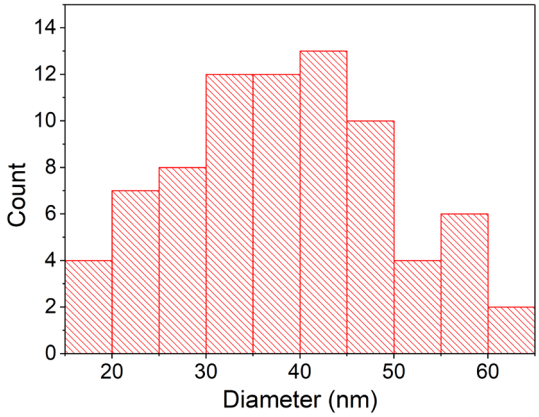

Figure S7. Size distribution of NiFeSi-12

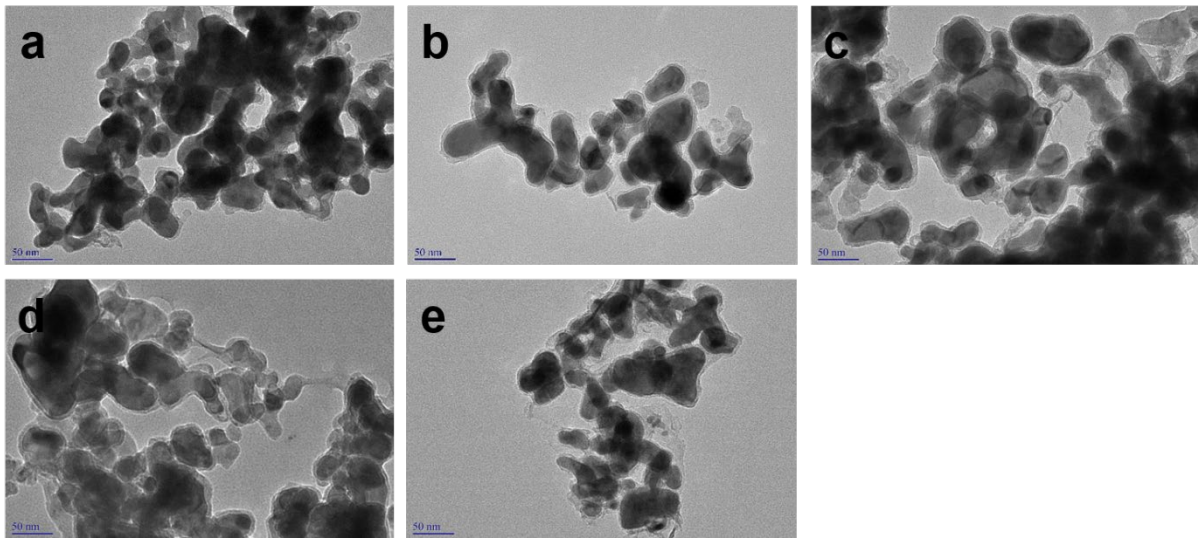

Figure S8. TEM images of (a) NiFeSi-50, (b) NiFeSi-12, (c) NiFeSi-3, (d) FeSi and (e) Ni_2Si.

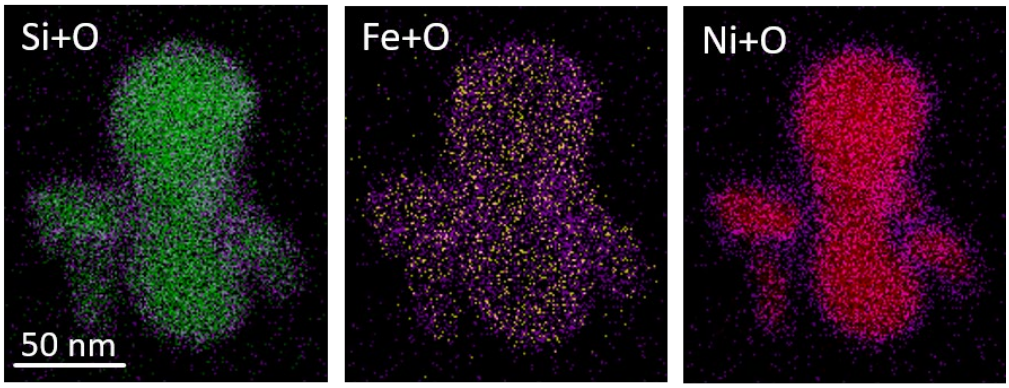

Figure S9. STEM-EDS mapping of the as-prepared NiFeSi-12 sample: superposition of oxygen and other elements. Si, Fe, Ni, O distributions are shown in green, yellow, red and purple, respectively.

Table S3. Elements atomic ratio of as-prepared Ni, Fe and NiFe silicide samples determined by EDX-SEM. The samples exhibit an excess of silicon compared to the composition expected from XRD phase identification. We then attribute this excess of silicon to amorphous silicon or oxidized silicon observed at the surface of the particles.

	Ni_2Si	NiFeSi-50	NiFeSi-12	NiFeSi-3	FeSi
Ni	1.68	1.96	1.85	0.84	/
Fe	/	0.04	0.15	0.31	0.58
Si	1	1.17	1.74	1	1

Electrochemical experiments

Electrode preparation. A Pt wire and Ag/AgCl in saturated KCl electrode were respectively used as counter electrode and reference electrode for a typical three-electrode configuration. There are two types of substrates used for the working electrode in this work. A glassy carbon (GC) rotating disk electrode (RDE) with a diameter of 5 mm was used for cyclic voltammetry (CV), linear sweep voltammetry (LSV) and electrochemical impedance spectroscopy (EIS) measurements, and a GC sheet was used for chronopotentiometry (CP) measurements. All catalyst inks were prepared with the same protocol. 3.4 mg of catalyst was sonicated in 480 μL absolute ethanol for 15 min, followed by adding 20 μL of Nafion solution (5% in alcohols and water, Sigma-Aldrich) for another 10 min of ultrasonication. A given volume of well-dispersed ink was dropped onto the GC sheet or the as-polished RDE substrate to obtain a catalyst loading of 170 $\mu g_{catalyst}/cm^2_{electrode}$, and then the substrate was dried for at least 30 min under air. IrO_2 nanoparticles were deposited according to the same protocol.

Electrolyte purification. *ca.* 1 g of as-prepared $Ni(OH)_2$ solid was put into 200 mL as-prepared 0.1M KOH. The suspension was sonicated for 3 min and then rested for at least 6 h. The purified 0.1M KOH supernatant was separated by centrifugation, stored under nitrogen and later used as electrolyte.

Electrochemical measurements. A home-made PMMA electrochemical cell was used for all measurements. The electrolyte was bubbled by O_2 for at least 20 min before measurement and during the measurement. The rotating rate of the RDE was set at 1600 rpm for all cyclic voltammetry (CV) measurements. CV and LSV measurements were performed at scan rate of 20 and 10 mV s^{-1}, respectively, from 0 to 1.0 V vs. Ag/AgCl in saturated KCl (equivalent to 1.0-2.0V vs. RHE). For the chronopotentiometry (CP), the current density was set at 10 mA cm^{-2} to monitor the potential evolution. Since a non-rotating GC sheet was used as working electrode substrate, a Teflon-covered stir bar stirred the electrolyte at 350 rpm during the measurements to decrease the limitation on activity due to ion depletion. The electrochemical impedance spectroscopy (EIS) was recorded in a frequency range of 50 000 to 1 Hz with a voltage amplitude of 10 mV.

Data treatment. For all potentials reported in this work, the ohmic drop iR was compensated, where the resistance is approximately equal to the total impedance measured at a frequency of 50 kHz. The potentials vs. RHE are obtained from conversion of measured potentials based on the equation: $E_{RHE} = E_{measured} + 0.197 + 0.0591 \times pH$, where pH = 13.

Cyclic voltammetry study

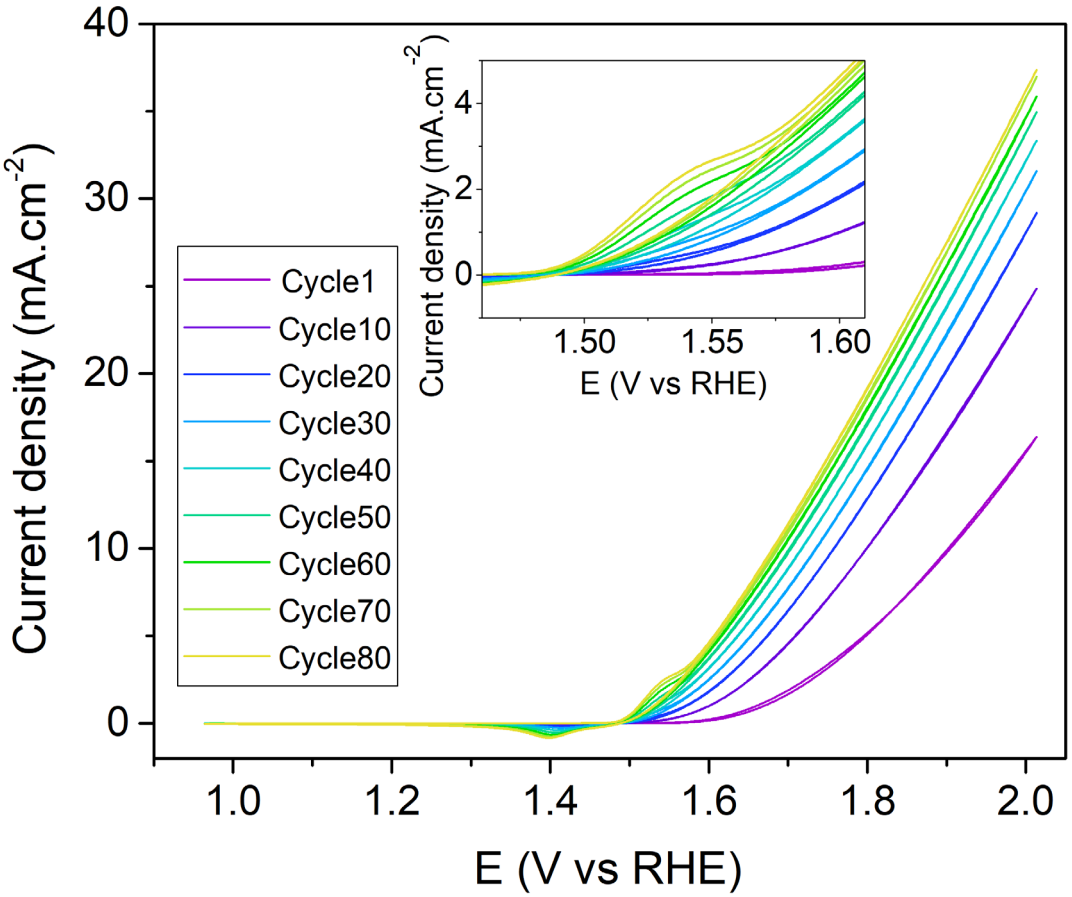

Figure S10. CVs for electrochemical activation of NiFeSi-12 by continuous potential cycling from 0.96 to 2.01 V vs. RHE at 20 mV s^{-1} in O_2-saturated 0.1 M KOH.

Electrochemical impedance spectroscopy study

In the Nyquist plots (**Figure S11**), the diameter of the semicircle in the high frequency region independent of the applied potential (**Figure S12**) represents the charge transfer resistance R_{ct}. The Fe-poor NiFeSi-50 exhibits the smallest R_{ct} (**Figures S11**). R_{ct} increases with the Fe content of NiFe silicides. The second semicircle in the low frequency region that decreases with the applied potential corresponds to R_{ads} (**Figure S12**). From **Figure S11,** the R_{ads} values are very close for the three NiFe silicides, which indicates similar surface states for these materials during electrocatalysis. The low values R_{ct}+R_{ads} (**Figures S10)** highlight the low overall resistances of NiFe silicide catalysts.

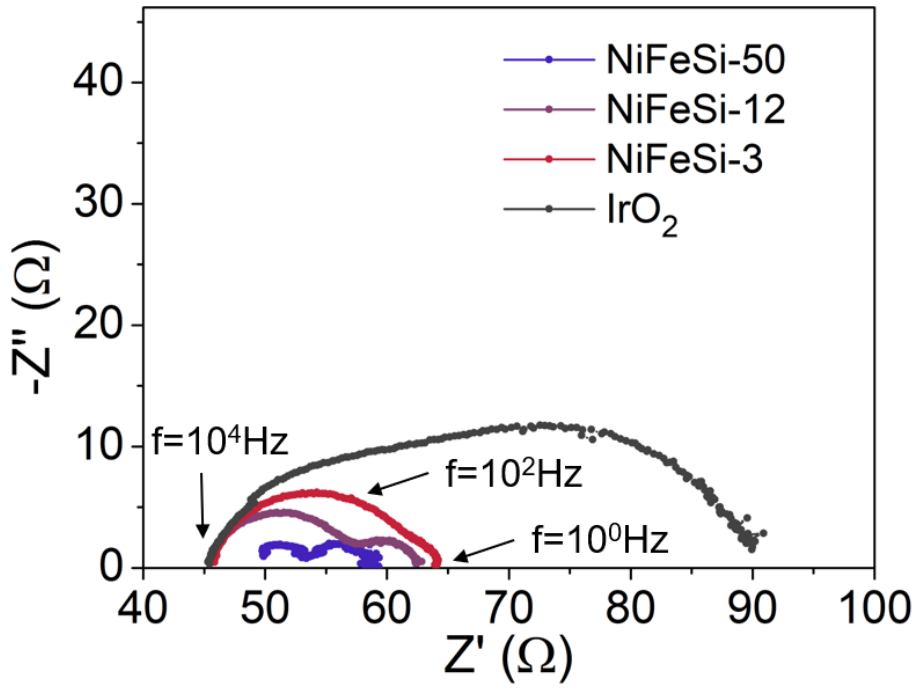

Figure S11. Nyquist plot recorded under 1.60 V vs. RHE of metal silicide nanocrystals and reference commercial IrO_2 nanoparticles in O_2-saturated 0.1 M KOH electrolyte.

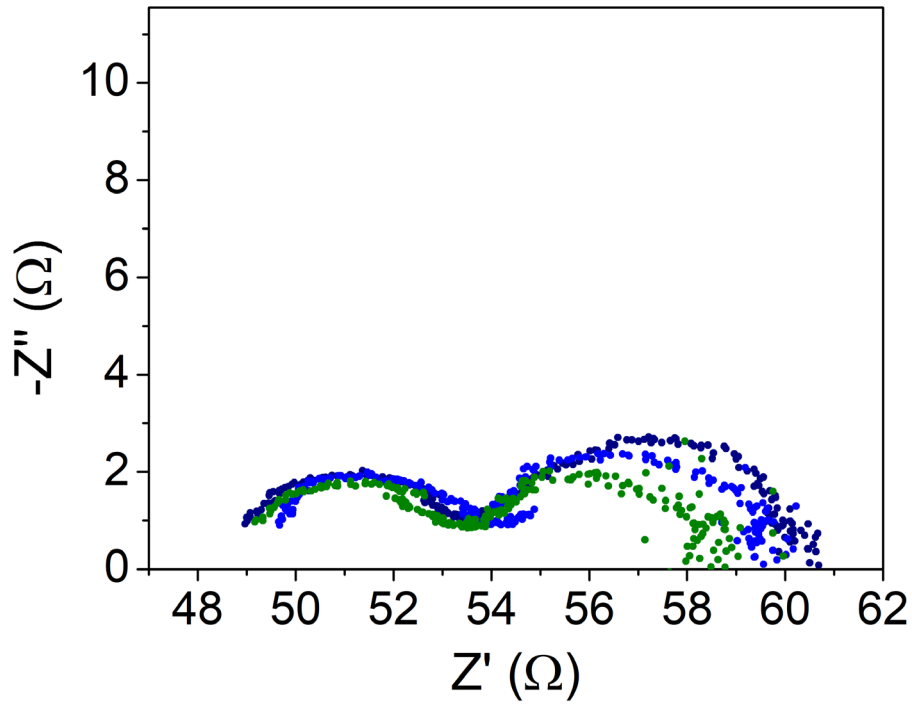

Figure S12. Nyquist plot of electrochemical impedance spectroscopy of NiFeSi-50 recorded at different potential from 50 000 to 1 Hz in green, blue, navy dots respectively, for 1.60 V, 1.59 V and 1.58 V vs. RHE**.**

Performance comparison of NiFe silicides with reported NiFe-based catalysts

Table S4. OER electrocatalytic activity and stability of previously reported NiFe-based catalysts in **0.1 M KOH** on **GC substrate**.

Catalyst	Loading amount (mg cm^{-2})	Overpotential (mV) @10mA cm^{-2}	Stability (h)	Tafel slope (mV dec^{-1})	Ref
NiFeSi-50	**0.17**	**337**	**85**	**63.8**	**This work**
NiFeSi-12	**0.17**	**345**	**85**	**85.4**	**This work**
NiFeSi-3	**0.17**	**393**	**85**	**75.3**	**This work**
nNiFe-LDH/NGF[a)]	0.25	337	3.3	45	[9]
Amorphous $Ni_{70}Fe_{30}(OH)_x$	0.14	292	2	30.4	[10]
$NiFe_2O_4$/α-$Ni(OH)_2$[b)]	~0.2	340	2.7	41	[8]
Ni_3FeN	~0.13	355	3.3	70	[11]
Fe^{3+}-doped β-$Ni(OH)_2$	0.25	260	10	32	[12]
NiFe-N/C[c)]	0.40	320	2000 cycles	44.2	[13]
NiFe-NC[d)]	0.20	380	2.8	115	[14]
graphene/NiFe (oxy)hydroxides	0.25	372	2.2	76	[15]
$Ni^{II}Fe^{III}$@NC	0.29	397	12	81	[16]
NiFe-LDH NS[e)]	0.14	290	8	33.4	[17]
Porous NiFe Oxide	0.14	328	12	42	[5]
$Ni_2Co^{III}Fe$-LDH/N-GO[f)]	0.18	317	8.3	74.1	[18]
Ni_3Fe/N-C	0.13	370	3.3	77	[19]
NiFe/C	0.50	330	21	57	[20]
m-NiFe/CN_x	0.51	360	5.6	59.1	[21]
NiFe LDH/oGSH[g)]	0.25	350	2.8	54	[4]
NiFe LDH	0.10	360	2	51	[22]
NiFe@NC_X	0.40	320	10	60.6	[23]

[a)] NGF: N-doped graphene framework
[b)] 0.1M NaOH
[c)] N/C: bimetal-decorated, pyridinic N-dominated large-size carbon tubes
[d)] NC: MM′ alloy and nitrogen-codoped porous carbon
[e)] NS: layered double hydroxide (LDH) nanosheets (NSs, ~ 1.3 nm)
[f)] N-GO: nitrogen-doped graphene oxide
[g)] oGSHs: oxidized graphene/ single-walled CNT hybrids

Table S5. Comparison of charge transfer resistance (R_{ct}) and mass transfer related to reaction intermediates adsorbed at the electrode surface (R_{ads}) for NiFeSi-12 electrodes in different stages of electrolysis.

Electrode	As-prepared	After 20 CVs	Post 85h-OER
R_{ct} (Ω)	6.2	5.3	5.2
R_{ads} (Ω)	15	6.9	0.1

Post mortem study of NiFe silicides

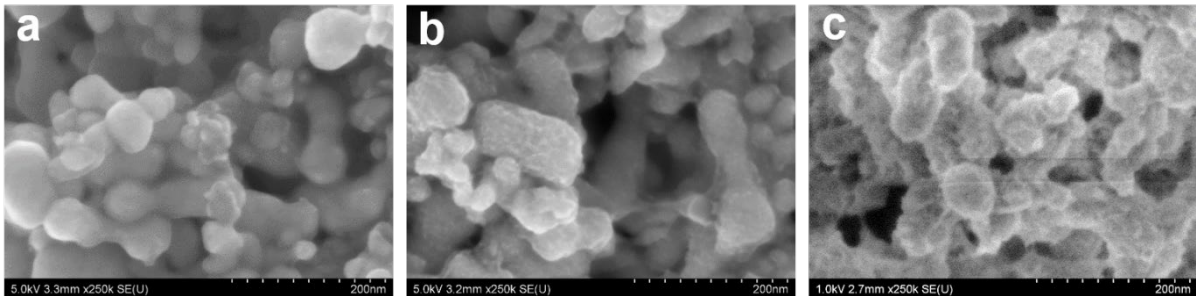

Figure S13. SEM images of a working electrode made of NiFeSi-12 nanoparticles deposited on a GC substrate (a) before electrochemical study, (b) post 10h OER, and (c) post 85h OER.

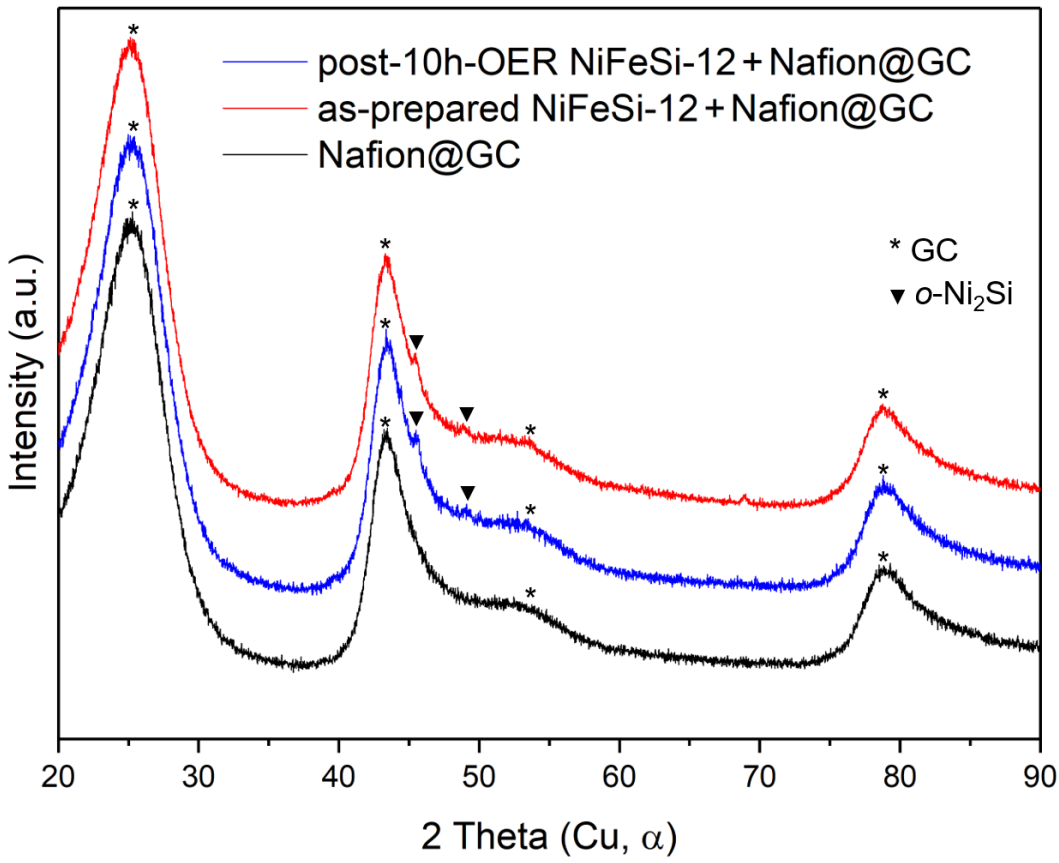

Figure S14. XRD patterns of a NiFeSi-12/glassy carbon electrode as-prepared and *post mortem* after 10 h of OER at 10 mA cm^{-2}. The pattern of a blank electrode without catalyst is shown as reference.

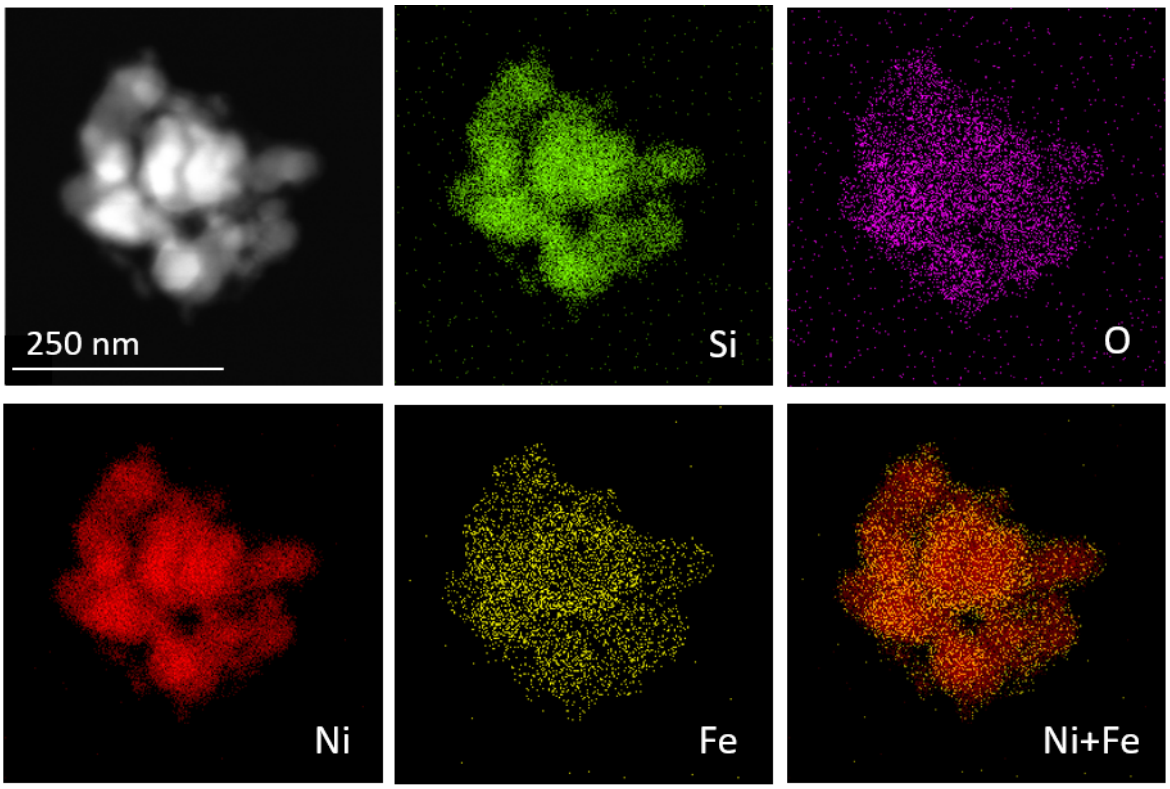

Figure S15. STEM-EDS mapping of NiFeSi-12 catalyst post 10h OER at 10 mA cm^{-2}.

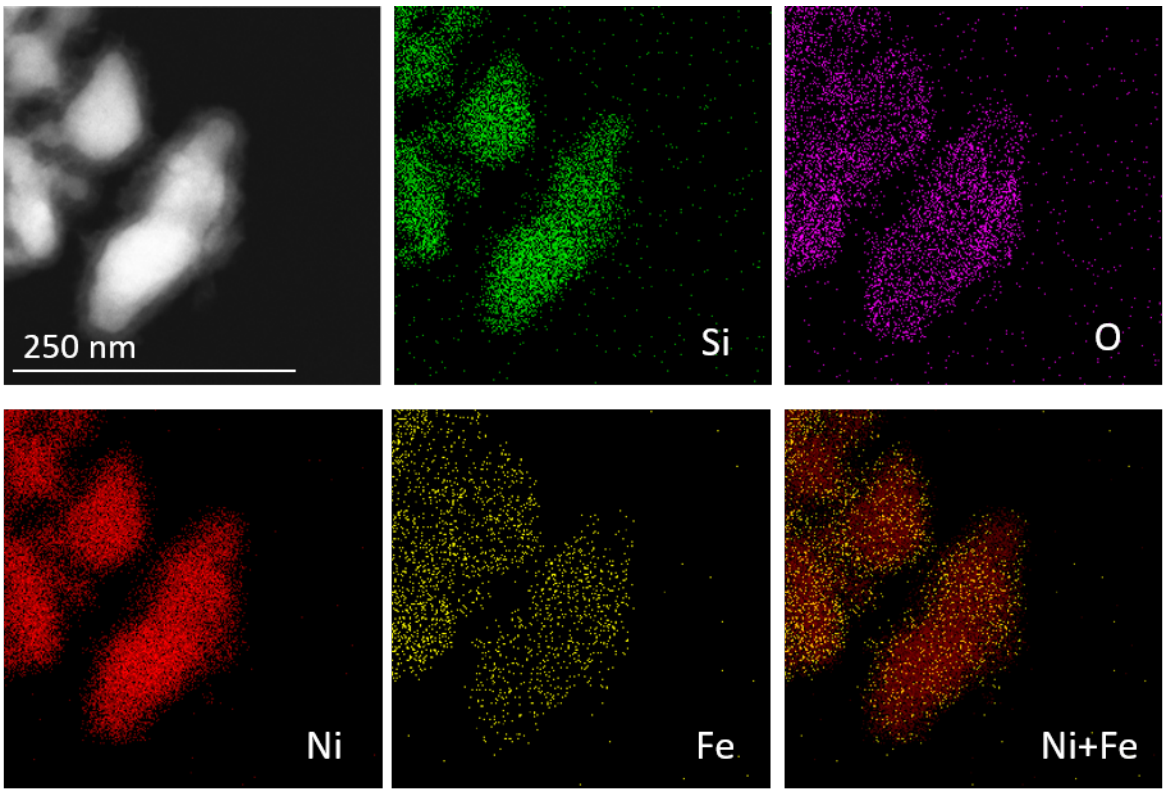

Figure S16. STEM-EDS mapping of NiFeSi-12 catalyst post 65h OER at 10 mA cm^{-2}.

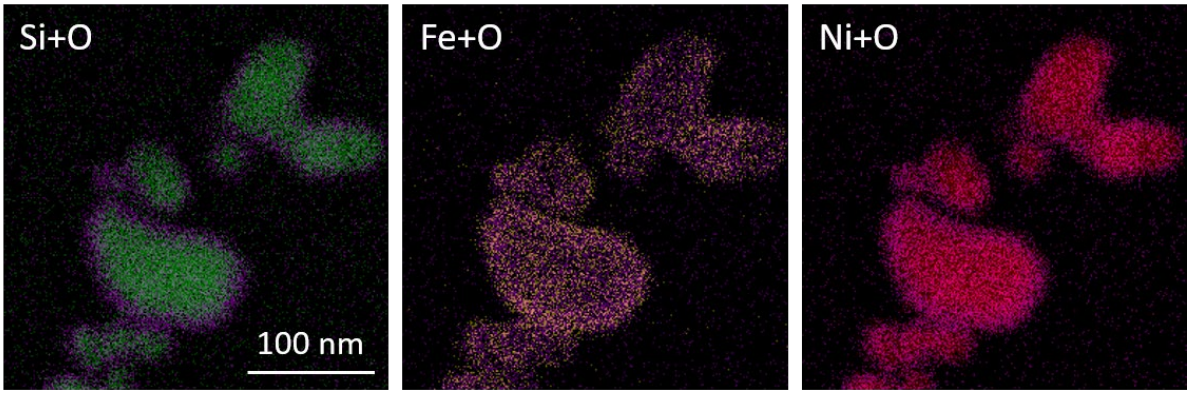

Figure S17. STEM-EDS mapping of NiFeSi-12 catalyst post 85h OER at 10 mA cm^{-2}: superposition of oxygen and other elements. Si, Fe, Ni, O distributions were shown in green, yellow, red, purple dots, respectively.

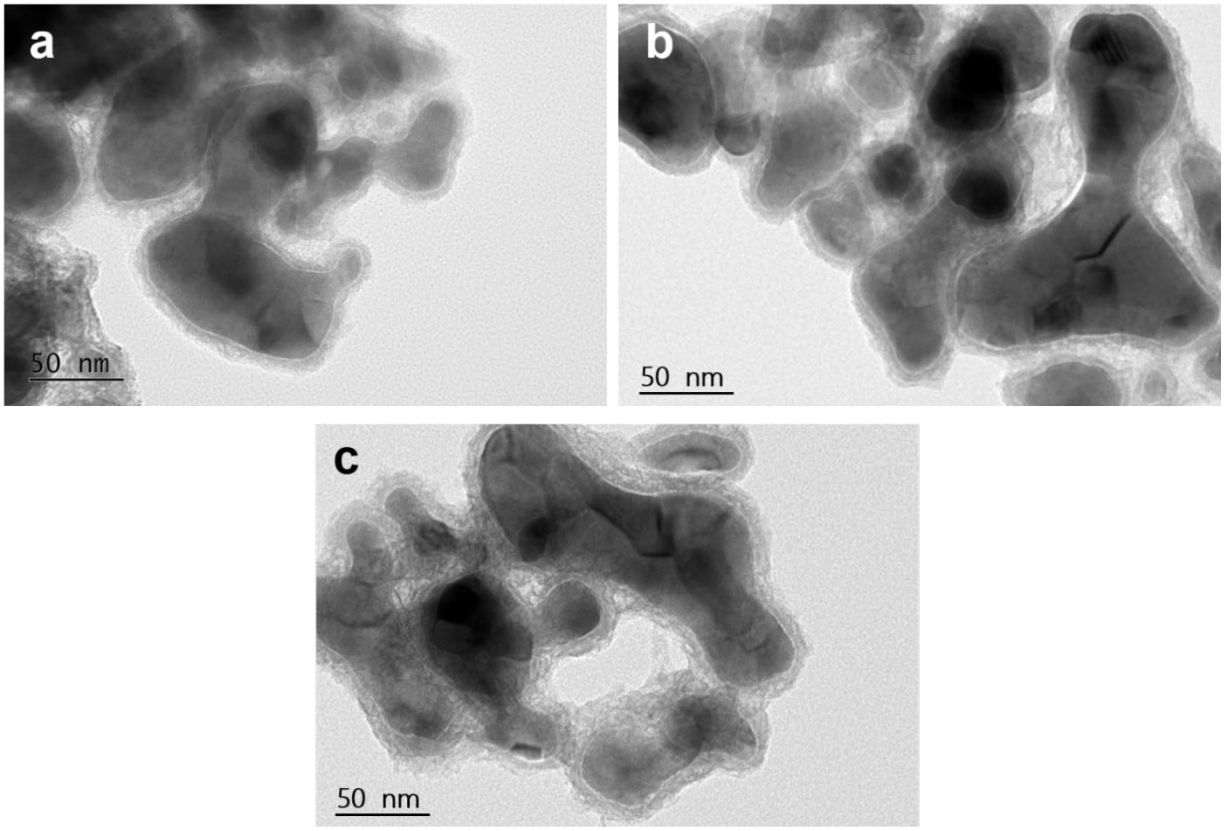

Figure S18. TEM images of NiFeSi-12 catalyst (a) post 10h OER, (b) post 65h OER, (c) post 85h OER at 10 mA cm^{-2}.

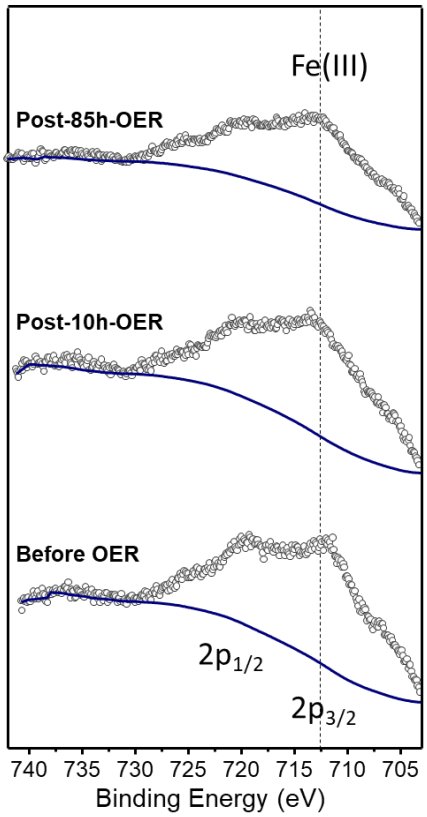

Figure S19. XPS analysis of the Fe 2p region for a NiFeSi-12 working electrode before OER, post 10h OER and post 85h OER.

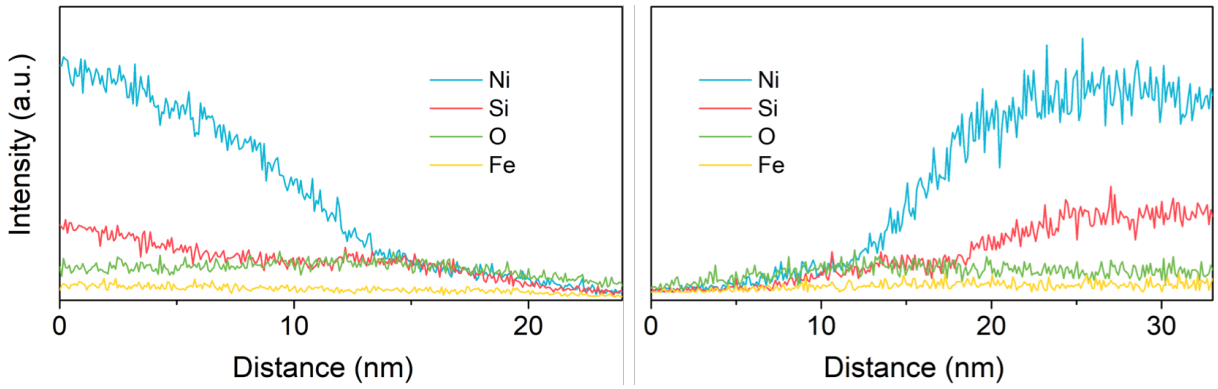

Figure S20. STEM-EDS line profile mapping of two NiFeSi-12 particles post 85h OER at 10 mA cm^{-2}.

Table S5. Elemental composition determined by SEM-EDS of a pristine NiFeSi-12 sample and of corresponding post mortem electrode materials after 65 and 85 h of OER operation.

	Pristine	Post 65h-OER	Post 85h-OER
Ni	1.85	1.85	1.85
Fe	0.15	0.12	0.11
Si	1.74	0.77	0.76

Supporting references

[1] C. Tang, H. Sen Wang, H. F. Wang, Q. Zhang, G. L. Tian, J. Q. Nie, F. Wei, *Adv. Mater.* **2015**, *27*, 4516.

[2] E. Lee, A. H. Park, H. U. Park, Y. U. Kwon, *Ultrason. Sonochem.* **2018**, *40*, 552.

[3] H. Chen, J. Yan, H. Wu, Y. Zhang, S. Liu, *J. Power Sources* **2016**, *324*, 499.

[4] G. Fu, Z. Cui, Y. Chen, L. Xu, Y. Tang, J. B. Goodenough, *Nano Energy* **2017**, *39*, 77.

[5] K. Zhu, H. Liu, M. Li, X. Li, J. Wang, X. Zhu, W. Yang, *J. Mater. Chem. A* **2017**, *5*, 7753.

[6] J. Wang, F. Ciucci, *Small* **2017**, *13*, 1.

[7] L. Yang, X. Zeng, D. Wang, D. Cao, *Energy Storage Mater.* **2018**, *12*, 277.

[8] C. Tang, H. F. Wang, H. Sen Wang, F. Wei, Q. Zhang, *J. Mater. Chem. A* **2016**, *4*, 3210.

[9] L. Du, L. Luo, Z. Feng, M. Engelhard, X. Xie, B. Han, J. Sun, J. Zhang, G. Yin, C. Wang, Y. Wang, Y. Shao, *Nano Energy* **2017**, *39*, 245.

[10] R. Gao, D. Yan, *Nano Res.* **2018**, *11*, 1883.

[11] J. Qi, W. Zhang, R. Xiang, K. Liu, H. Y. Wang, M. Chen, Y. Han, R. Cao, *Adv. Sci.* **2015**, *2*, 1.

[12] D. Zhou, Z. Cai, X. Lei, W. Tian, Y. Bi, Y. Jia, N. Han, T. Gao, Q. Zhang, Y. Kuang, J. Pan, X. Sun, X. Duan, *Adv. Energy Mater.* **2018**, *8*, 1701905.

[13] G. Fu, Z. Cui, Y. Chen, Y. Li, Y. Tang, J. B. Goodenough, *Adv. Energy Mater.* **2017**, *7*, 1.

[14] C. Andronescu, S. Barwe, E. Ventosa, J. Masa, E. Vasile, B. Konkena, S. Möller, W. Schuhmann, *Angew. Chemie - Int. Ed.* **2017**, *56*, 11258.

[15] S. Ci, S. Mao, Y. Hou, S. Cui, H. Kim, R. Ren, Z. Wen, J. Chen, *J. Mater. Chem. A* **2015**, *3*, 7986.

[16] X. Zhu, C. Tang, H. F. Wang, Q. Zhang, C. Yang, F. Wei, *J. Mater. Chem. A* **2015**, *3*, 24540.

[17] F. Dionigi, T. Reier, Z. Pawolek, M. Gliech, P. Strasser, *ChemSusChem* **2016**, *9*, 962.

[18] J. Zhu, M. Xiao, Y. Zhang, Z. Jin, Z. Peng, C. Liu, S. Chen, J. Ge, W. Xing, *ACS Catal.* **2016**, *6*, 6335.